Title
Investigation of Germanium Nanoparticles and Metal-Halide Perovskites in Optoelectronics

Author
Sfadia, Roy Mattan

Publication Date
2022

UNIVERSITY OF CALIFORNIA
SANTA CRUZ

INVESTIGATION OF GERMANIUM NANOPARTICLES AND METAL-HALIDE PEROVSKITES IN OPTOELECTRONICS

A dissertation submitted in partial satisfaction of the
requirements for the degree of

DOCTOR OF PHILOSOPHY

in

PHYSICS

by

Roy M. Sfadia

March 2023

The Dissertation of Roy M. Sfadia
is approved:

Professor Sue. A. Carter, Chair

Professor Frank Bridges

Professor Jairo Velasco

Peter F. Biehl
Vice Provost and Dean of Graduate Studies

Table of Contents

List of Figures v

List of Tables x

Abstract xi

Acknowledgments xiii

1 All the theory 1
- 1.1 Bulk Crystal Theory 1
  - 1.1.1 Crystallography 2
  - 1.1.2 Germanium and the Diamond Crystal Structure 5
  - 1.1.3 Perovskite Crystal Structure 5
- 1.2 Bandgap Theory 8
- 1.3 Quantum Dots 12
- 1.4 Device Physics Theory 14

2 Experimental Methods 19
- 2.1 Fabrication Techniques 19
  - 2.1.1 Spin-Coating 20
  - 2.1.2 Doctor Blading 21
  - 2.1.3 Thermal Evaporation 22
- 2.2 Characterization Techniques 22
  - 2.2.1 Photoluminescence Spectroscopy 22
  - 2.2.2 Absorption Spectroscopy 23
  - 2.2.3 Atomic Force Microscopy 25
  - 2.2.4 Current-Voltage Measurements 27

3 **Simulation of Raman Spectrum for Germanium Quantum Dots** **28**
3.1 Background & Theory 29
3.2 Modeling Germanium Quantum Dots 35

4 **Ge QD photodetectors** **45**
4.1 Background 45
4.2 Experimental Methods 46
4.3 Results 49
4.3.1 Bandgap Estimates 49
4.3.2 Urbach Energy Estimates 50

5 **Thickness Study of Hole Transport Layer in Planar $MAPbI_3$ Solar Cell** **52**
5.1 Device Architecture 54
5.1.1 Layer Motivation 54
5.1.2 Device Fabrication 56
5.2 Device Performance 59
5.2.1 PEDOT:PSS Thickness 60

6 **Organic-Inorganic Perovskites in Light-Emitting Diodes** **68**
6.1 Introduction 69
6.2 Previous work on PeLEDs 71
6.2.1 Comparing and Constrasting Solar Cell Optimization . . . 71
6.2.2 Tunability through Composition 73
6.3 Device Fabrication 75
6.3.1 SpiroOMeTAD Preparation: 75
6.3.2 Perovskite Preparation 75
6.3.3 Perovskite Film Fabrication 76
6.3.4 Device Fabrication 76
6.4 Work and Results 77
6.4.1 Device Architecture 77
6.4.2 Exploring Perovskite Preparation and Stoichiometry . . . 81
6.4.3 Optimizing Anti-Solvent Drop Time 84
6.4.4 Trap States as a Function of Stoichiometry 85
6.4.5 Device Performance 88

7 **Conclusion** **90**

Bibliography **93**

A **Calculating Volume-to-Surface Ratio** **104**

List of Figures

1.1 Left and center panels show the same grove of trees, first along the farm's lattice vector, and then not. The right panel shows a diagram of the same concept. 4
1.2 Three common conventional unit cells. Lattice constants a, b, and c represent the dimensions of the cell. If $a = b = c$, we say the cell is cubic. 4
1.3 Two crystal structures that describe much of materials discussed in this work. 6
1.4 The splitting of energy levels as one adds potential wells. These results were obtained using the applet available at CU Boulder's PhET project. 9
1.5 From left to right: a schematic of a semiconductor's energy bands, the density of states as a function of energy levels, the fermi-dirac distribution for $T > 0$, and finally the carrier concentration, which is a mathematical product of the fermi-dirac distribution and the density of states. The second row depicts the increase in electron carrier concentrations when the semiconductor is negatively doped. Adapted from Reference [1]. 11
1.6 A bound electron-hole system, depicting the size of the exciton relative to the lattice spacing. 12
1.7 A plot of several group's mean particle size and respective bandgap. Adapted from Reference [2]. 14

1.8 A metal-semiconductor junction. As the contact becomes intimate, electrons flow from the material with the smaller work function to the material with the larger work function. This results in an electric field at the interface. For $(\chi + \phi_n) < \phi_m$ (where χ is the semiconductor's electron affinity, ϕ_n is the energy difference between the conducting edge and the fermi energy, and ϕ_m is the metal's work function) the resulting space charge acts as a rectifying boundary. Adapted from chapter 3 of Sze's *Physics of Semiconducting Devices*Reference [15]. 17

1.9 "Bandgap Heaven", a compilation of conduction edges, valence edges, and work functions for various metals, semiconductors, and insulators. Device physicists often reference such documents for guidance on device architecture. 18

2.1 **a)** Spin coating steps, including a1) the deposition of a solution, a2) the initial acceleration of the platform, a3) when the platform reaches a steady-state speed ω and volume is lost due to centrifugal forces, and a4) where volume is now lost primarily through evaporation. **b)** Doctorblading, where one simply drags the sample in a crevice or well to form a layer to be dried. 21

2.2 Normalized curves of both photoluminescence and absorbance for $FAPbBr_3$. As expected, the photoluminescence peak coincides with the absorption edge. 23

2.3 a) A 10µm x 10 µm AFM profile of $MAPbI_3$ used to measure roughness. b) An AFM profile of a razor blade score on PEDOT:PSS. c) an optical photograph of the razor blade score on the surface of a sample. 26

3.1 a) An energy-level diagram depicting rayleigh/elastic scattering and inelastic/Raman scattering. b) An experimentally acquired Raman spectrum for a bulk germanium wafer. Its peak sits at 301 cm^-1. 30

3.2 A figure depicting calculated (solid lines) and experimentally determined (markers) germanium dispersions. One can see at $k = 0$, represented by the Γ line, six phonon modes. There are three acoustic modes at the bottom, and three optical modes at the top. There is much degeneracy among these phonon groups, especially about Γ, though one can see the degeneracy break in the leftward phonon modes towards the X line. For all three optical modes, the negative slope about Γ predicts access to lower frequency modes and therefore a red shift in spectra once selection rules are relaxed. Figure adapted from Reference [3]. 32

3.3 Bulk germanium (gray) sample compared to samples of large (blue) and small (red) quantum dots. As our dots get smaller, we get larger low-energy broadening. Initial high-energy broadening is likely due to strain between the crystalline core and the amorphous germanium shell. This is all collected data and not modeled. . . . 35
3.4 Two plots inspecting various variances for the weighting function $W(\vec{q},\vec{r}) = \exp\left[-\vec{r}^2/(2\sigma^2)\right]$ for dots of average crystallite size a) 3.1 nm and b) 8.7 nm. These dots were synthesized using an iodine precursor as described in Reference [4]. These calculations do not consider size distributions. These were calculated Using Equation 3.6. 40
3.5 Graph showing the difference between a log-normal and a normal distribution given the same population mean and variance. Here, $\mu = 3.1$ and $\sigma = 0.8$. 42
3.6 Raman spectra (black crosses) and models with varied parametes. All models use the same weighting function and weighting function variance. However, they vary in the implementation of the size distribution. The light, dashed lines show fits when we consider the XRD results, which suggest fitting to 3.1 nm. The solid lines 44

4.1 High-resolution tunneling electron microscopy images of highly-crystalline germanium nanocrystals, fabricated by Ju et. al. *via* novel two-step synthesis method. Adopted from from [5]. 47
4.2 Device architecture of our germanium quantum dot photodetectors 49
4.3 Left: Photothermal deflection spectroscopy of various quantum dot sizes. Listed are particle size, as determined by HAADF-STEM, and their corresponding crystallite size, as determined by fits to XRD results. Right: Urbach energy values, calculated *via* the reciprocal of the slope the intermediary linear region on a plot of $\log(\alpha)$ *vs* $h\nu$. 50

5.1 a) energy level diagram for our perovskite solar cell. While hole transport layers have well documented work functions, the LUMO level of PCBM is disputed. Polycrystalline Ag has a work function of 4.3 eV, but a thin layer of LiF forms a dipole moment that benefits device performance. b) The device architecture in planar form. Thicknesses are not to scale. 55

5.2 Atomic force microscope measurements of area A 10 µm x 10 µm for (a) two-step $MAPbI_3$ layer without an IPA wash, b) a similarly prepared $MAPbI_3$ layer with an IPA wash. Mean roughness measurements indicate that the IPA wash halves the surface roughness, decreasing trap states that would be found at the $MAPbI_3$/PCBM interface. 57
5.3 Some choice current-voltage measurements from various PEDOT:PSS dilutions. From the top-left corner towards the bottom-right, we get a progression of increasingly diluted solutions producing better devices. Note that our hero device, the solid blue line with a PCE of 19%, had a more optimized PCBM layer as well. 61
5.4 Plotted here are the (a) power conversion efficiencies, (b) fill factors, (c) the short circuit currents, and (d) the open-circuit voltages for devices fabricated with no PEDOT:PSS layer, with 400% dilution, 300% dilution, 200% dilution, and with PEDOT:PSS as is. Lightest blue corresponds to most dilution (i.e. no PEDOT:PSS) to darkest blue with no dilution. 62
5.5 Two PEDOT:PSS thin-films prepared on glass, a) as-shipped and b) diluted to twice the volume. Upon further dilution, AFM measurements became unreliable. 63
5.6 Voltage-vs-current measurements on PEDOT:PSS thin-films of various dilutions. These measurements were made *via* a 4-point probe on 1 in^2 glass susbtrates. The subwindow shows a close-up of the non-dilution trace on a different scale, as it appears flat on the voltage range needed to display the diluted films. 65

6.1 Schematics of (A) edge-to-edge recombination, (B) "hot" electron relaxation, emitting a photon $E_\gamma > E_{\mathrm{BG}}$, (C) shallow and deep trap states that prevent radiative recombination. 70
6.2 Summarizes the peak emission wavelength of various PeLEDs along with their respective quantum efficiencies. From Reference [6], with literature sources tabulated in the paper's supplementary information document. 74
6.3 The energy levels associated with the two device architectures explored, with a) often referred to as as reverse architecture, and b) the more conventional architecture. 79

6.4 A semi-log J-V plot showcasing an ensemble of devices using the p-i-n (purple) and n-i-p (yellow) architectures. We see that, for low currents, the p-i-n architecture magnitudes more of current. The lack of proper blocking layers in the p-i-n architecture might lead to current passing through the device without recombination. The subfigure showcases the same plot on linear axes. The green line highlights the bandgap voltage 2.3 V for $FAPbBr_3$. 80
6.5 a) Schematic of the one-step solvent engineer process spearheaded by Jeon *et. al.* [7]; this diagram is borrowed from their work. b) $FAPbBr_3$ film spun on glass, with and without UV light. 82
6.6 a) the photoluminescence and absorption spectrum of $FAPbBr_3$ found by Wang *et. al.*[8]. b) My own spectroscopy measurements, finding an identical spectrum. 83
6.7 Roughness measurements for $FAPbBr_3$ composed with a) 0% excess FABr, b) 20% excess FABr, and c) 100% excess FABr. Note that each Figure is scaled to its own range of values, so the stoichiometric sample's spikey appearance is in fact smooth. 83
6.8 $FAPbBr_3$ thin films with and without an anti-solvent drop 4s after beginning to spin the substrate. We see a 5x decrease in surface roughness when an anti-solvent is used. A smooth surface is an important condition for charge injection and radiative recombination. 84
6.9 Toluene anti-solvent drop times at t = 3s (red), 4s (yellow), and 5s (green) for samples with 0% to 50% excess FABr. We see that for nearly all samples, a 4s drop time is the most effective for maximizing photoluminescence. 86
6.10 Photothermal deflection spectroscopy results for $FAPbBr_3$ films prepared with 0-50% excess FABr precursor. Fitted with a direct tauc plot, all samples measured an optical bandgap of 2.8 eV. . . 87
6.11 a) A schematic showing that the photocurrent is producing light which is being measured by a photodiode; b) The photocurrent produced by the photodetector (green), measuring the quantity of light being produced by the working PeLED's injected current (brown); c) Electroluminescence spectra with a Full-Width-Half-Maximum of 24 nm, and inset photograph of an operating PeLED; d) CIE plot showing high color purity of 540 nm. 89

A.1 A crystal of uniform length, width, and height $\mathcal{L}$. 105

List of Tables

3.1 Crystallite sizes for various precursor molarities. 36

4.1 The three samples being investigated in this work. Whereas the monocrystalline samples have crystallite sizes comparable to their particle size, the polycrystalline dots' have a discrepancy between particle size and crystallite size. 47

5.1 Extrapolated thickness values keeping ρ_0 constant. We see very dubious results for relative concentrations that span only half an order of magnitude. 67

5.2 Extrapolated thickness from the 1:1 value, assuming a linear relationship between concentration and thickness. We see very extreme changes in resistivity for relative concentrations that span only half an order of magnitude. 67

Abstract

Investigation of Germanium Nanoparticles and Metal-Halide Perovskites in Optoelectronics

by

Roy M. Sfadia

Thin-film optoelectronics are an incredibly worthwhile research topic. Unsurprisingly, their thin profiles use less material than their thicker, more traditional counterparts. However, they also benefit from increased flexibility, as well as an increased array of fabrication routes. The materials investigated in this work are well poised for scalable solution processing techniques that lend themselves to a manufacturing setting.

Here, I investigate three types of optoelectronic devices: a) the photodetector, b) solar cells, and c) and light-emitting diodes (LEDs). All of these work to transform between light particles and electronic particles. My work examines, in each case, what makes for a successful device.

Beginning with germanium quantum dots, this work begins by modeling the Ge QD raman spectra as a function of particle size. To do this, we implement the confined phonon model first implemented by Richter, Wang, and Ley[18]. We succesfully predict the extreme asymmetric broadening towards low-energy modes that is observed in data taken by collaborators.

We then implemented Ge QDs into thin-film photodetectors, using an ITO/ TiO_2/Ge QD/Au architecture. We found a signal-to-noise a ratio greater than 10^4 at at 1V bias. Additionally, it was found that conductivity was improved by Ge QDs samples with increased crystallinity.

Our next study focused on thin-film organic-inorganic perovskite solar cells. Using methylammonium lead iodide ($MAPbI_3$) as our absorption layer, these devices utilize a well-studied architecture which uses PEDOT:PSS as a hole extraction layer. We find that increasingly thinner PEDOT:PSS layer results in better performing devices.

My last chapter focuses on using formamidinium lead bromide ($FAPbBr_3$) as a green-emitting active layer in an ITO/TiO_2/Perovksite/Spiro-OMeTAD/Au architecture. By reducing the free lead content in our system *via* a nonstoichiometric precursor ratio, we find successful green emission despite increased disorder on the perovskite surface.

Acknowledgments

After being a professional student for so long, having completed my bachelor's degree and master's degrees back-to-back, it is quite a shock to the ego to embark on a research project of my own. For eighteen years, I struggled on homework and tests; I would eagerly await the day the assignments were handed back, devouring what the red ink had to say so I could find out what the Right Answers were. Finally, halfway through "18th grade", I was assigned one more assignment: a Ph.D. thesis, for which there is no answer in the back of the book. In fact, there wasn't yet a question that demanded an answer. It is up the the doctoral student to come up with a question worth asking, and to deliver an answer. It is safe to say that without the support system I have had before and during this work, I would never have made it to this point.

Taking this chronologically, I have to first thank my family. My parents provided me and my brothers with a loving home, working hard to ensure that we had anything we wanted, while also teaching us that whatever we have is enough. Though I am the youngest of four, its true that at times I felt I was an only child raised by a half a dozen people. Being so much older than me, my brothers and sister-in-law had also taken ownership over my well-being. They entered the workforce and loved having the opportunity to splurge on their youngest brother; and despite being so much younger, they were always happy to take me to the movies, play video games, or sit me down for a lesson on their favorite album. I can not express enough gratitude towards my family, for not only accepting my geekiness, but celebrating it, and for always looking for avenues to encourage it. While they begrudgingly let me leave home to attend university, they quickly became so supportive and proud of my studies. For that I am grateful.

My childhood friends are also so important to me getting to where I am. Being a newly-minted physicist, I believe I will be fined for assigning randomness to anything except for nuclear decays, but I have no choice but to be thankful for whatever quantum fluctuations led me to the friendships I've had along the way here. Amit is a brother to me in all but genetics, and I am so curious what 18-month old me was thinking when he struck up a friendship with him (or did baby Amit approach me? How do children that can hardly identify the colors of the rainbow strike up conversation?). Bless whatever neutron decayed into a proton for situating the universe such that I met him, Christian, Max, Daniel, Zach, Aria, Jalen, and the rest of the family-you-choose I met in high school. I feel like we were all proto-planetary clumps in a chaotic nebula, bouncing off one another in the energy of childhood to help each other form proper shapes and stable orbits.

I would be remiss not to mention the people I met in college. Having no idea what differentiated one discipline from another, I entered San Francisco State a civil engineering major. Quickly I became aware that the reason I had chosen any engineering at all was because I enjoyed my physics classes (perhaps I was further encouraged by the Jerry Garcia bobble-head I eyed sitting in my physics professor's office hours). I'll never forget the first time I felt I made the right choice switching to physics, when Colin and I fell to the library floor laughing, having discovered that physics was "constants all the way down". [1]

Colin introduced me to our Physics and Astronomy Club, which became my fraternity and my bunker for two years. There I met Daniel, Ryan, Michelle, Sarah, and others who were comrades in the struggle to understand Schrodinger's Equation and the laws of thermodynamics.

While at State, I met professors that inspired me to grok the material in they way they seemed to. In particular, Physics professor Barbara Neuhauser was always one to hear me out in her office hours as I perspired and about whether or not to go to graduate school, and provided me the foundation to solid-state physics and analog electronics that was so important for my later thesis work. Chemistry professor Andrew Ichimura supervised my foray into research, allowing me into his physical chemistry group. There, I was introduced to the art of research and data analysis, and got to take part in graveyard shifts at SLAC gathering data on

---

[1] Having just learned Coulomb's Law, we became intrigued by this mysterious k term. A search on Wikipedia taught us that it was defined by other constants, the seemingly strange ϵ_0 sitting there in the denominator. Of course, we then pressed the blue hyperlink for Vacuum Permittivity to learn that ϵ_0 itself is a constant defined by μs and cs.

materials that also found their way into my dissertation.

Thank you to my advisor Sue for letting me join her research group. Her encouragement to pursue whatever research interests I had was instrumental in the exercise of my 'independent researcher' muscle. Thank you to Katie, Eli, Emily, and Mana for the endless hours of support, for hearing all of my hey-does-this-make-sense spiels, and camaraderie.

Graduate school would have been an empty venture were it not for my cohort, friends, and housemates (a three- circle venn diagram with much overlap). When I moved to Santa Cruz, I knew one person in the whole town. I am so extremely lucky to have moved into 216 Laurel, where I got to insert myself into the orbits of farther-along graduate students Graham, Dave, and Jake, who immediately made me feel indescribably welcomed to Santa Cruz. Naturally, the next group of people I got to know was my large cohort. Nearly 20-strong, and with half of us sharing a defunct-lab-turned-office, we got to know each other late into the night as we worked on deciphering what exactly J.D. Jackson thought should be so clear to the readers of his book. I am particularly grateful to Brent, Carolyn, and Nora for our near-daily lunches and communications that almost certainly extended our graduate school tenure but made it worthwhile all the same. Hikes and adventures (and beer and burgers) were not lacking thanks to Daniel, Dominic, and Zippy and other cohort mates that knew discussions of physics, teaching, and other topics only benefited from mild inebriation.

Finally, I am grateful to my partner Tatev Avtandilian, who has supported me through these trying times for the past three years. My best friend for nearly half my life, she has been an outsized force in my initial conditions that I will always appreciate, and I can not describe the joy she brings to me every day.

Chapter 1

All the theory

1.1 Bulk Crystal Theory

As the name suggests, solid-state physics is the study of a large collection (10^{21} or more) of atoms that are bonded rigidly and interact strongly with one another. Solid-state physics developed as its own field of research, separate from ”fundamental” physics, because we find there is *emergent phenomona* when you have such a collection of atoms; put conversely by Oxford physicist Steven Simon, we study it “because reductionism doesn’t work”[9].

Solid-state theory is a vast and ongoing field of research; a chapter section can not do it justice. Here, I hope to discuss topics relevant to the work that will be presented in later chapters of this dissertation. Topics discussed will be crystallography, band theory, and heterojunctions.

1.1.1 Crystallography

Crystallography is the study of identifying and measuring characteristics of a crystal. Crystals, when used in scientific literature, refers any solid material made of atoms or molecules that arrange themselves in a regularly repeating pattern. One might point out that a crystal is not regularly repeating - that eventually the crystal comes to an end where it meets air, vacuum, or another material. Thankfully, most atoms in a crystal are well within the bulk of the sample. Even if a crystal is a just a micrometer in each direction, and surface effects negligible 5 lattice constants deep, the ratio of atoms inside the crystal to atoms on the surface is 120:1. If the crystal is a millimeter in each direction, that ratio blows up to 120,000:1 (see Appendix A for calculations). We leverage the mostly-bulk population of a crystal by assuming every atom is in the bulk. This is mathematically reinforced by asserting *periodic boundary conditions*, or PBCs. Anyone who has played the game *Asteroids* or*Pac-Man* knows of PBCs! A 1-D crystal lattice would enforce PBCs by turning into a 'ring' of lattice points where the last atom is glued to the back of of the first atom. A 3-D crystal would become a hyper-tyroid where the top and bottom, left and right, and front and back sides all connect to one another. I will not bother trying to describe such imagery.

Thus, much of basic solid-state theory arises from the assumption of an infinite and periodic pattern of lattice points. A *lattice* is an infinite array of repeating lattice points, where the only requirement is that the "view" of the lattice is the same from every lattice point (see Reference [10], chapter 4 for more details). The lattice point is a geometric waypoint; it denotes where the pattern of the lattice repeats. We may use a lattice to describe a *crystal structure* by gluing a basis to each lattice point. A basis may be a single atom, a collection of atoms, or a molecule. Simply put, Crystal Structure = Basis + Lattice. The lattice provides the repetition, and the basis is the physical object being patterned at every lattice point.

Lattice vectors are the displacements needed to move from one lattice point to another. They were best described to me my professor Barbara Neuhauser, the instructor for my undergraduate solid-state physics course. She said, if you were ever to see a grove of crops being grown along the 5 highway, you know you are looking along the lattice vector when suddenly all the trees become aligned. A moment later, as your car moves along, the same trees appear disordered and no rows can be seen. An example of such a grove of trees and a schematic of a 2-dimensional lattice, are shown in Figure 1.1.

The last notable terminology is the *unit cell.* As the name implies, the unit cell is the fundamental volume that is repeatedly tiled though space. It contains the

Figure 1.1: Left and center panels show the same grove of trees, first along the farm's lattice vector, and then not. The right panel shows a diagram of the same concept.

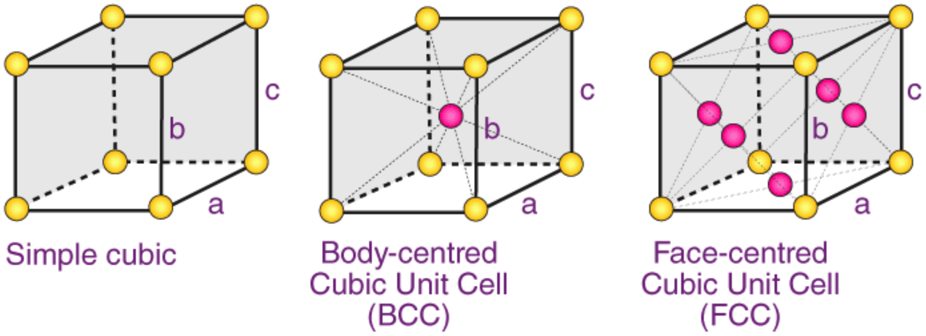

Figure 1.2: Three common conventional unit cells. Lattice constants a, b, and c represent the dimensions of the cell. If $a = b = c$, we say the cell is cubic.

basis atoms and their respective orientations to one another in space. Unit cells maybe be *primitive* unit cells, which is the minimum volume that can be tiled to succesfully descirbe the crystal, or more often they are a *conventional* unit cell, where a larger-than-necessary volume, one that more successfully showcases certain symmetries, is used. Figure 1.2 shows three common conventional unit cells.

I end this section by discussing the two crystal structures we will discuss in this work.

1.1.2 Germanium and the Diamond Crystal Structure

Being a Group IV element, germanium is naturally found in the *diamond structure*. Geometrically, the diamond structure is two overlapping face-centered cubic (FCC) lattices, each of lattice constant a, and one offset by the other by a distance of $a\frac{\sqrt{3}}{4}$ along the long diagonal of the unit cell. This is seen pictorially in Figure 1.3a.

With our 'Crystal Structure = Basis + Lattice' equation in mind, we construct the diamond crystal structure using the simple face-centered cubic, as seen in Figure 1.2, with a two-atom basis consisting of two atoms. The first atom sits atop the lattice point, and the other sits $\frac{a}{4}(\hat{x} + \hat{y} + \hat{z})$ away. If the second atom in the two-atom basis is a different element or compound from the first, this structure would be called a *zincblende* lattice.

1.1.3 Perovskite Crystal Structure

The perovskite structure is both simpler and more complicated. Its bravais lattice type is the simple cubic, though in some cases perovskite materials may have their unit cell distorted such that its sides are no longer cubic i.e. $a = b \neq c$

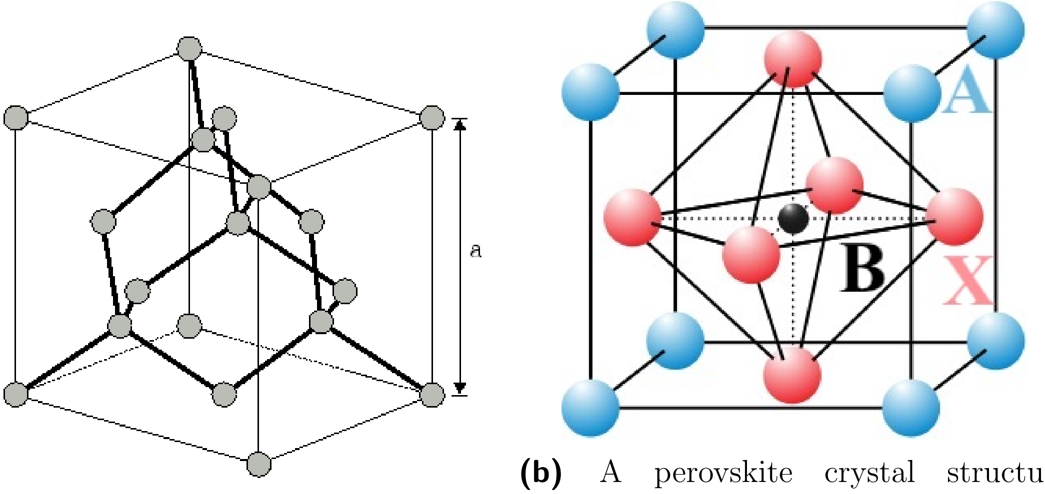

(a) A diamond crystal structure **(b)** A perovskite crystal structure (ABX_3).

Figure 1.3: Two crystal structures that describe much of materials discussed in this work.

(tetragonal) or $a \neq b \neq c$ (orthorhombic). The basis for the perovskite structure can be represented as ABX_3, where A^{+1} and B^{+2} are monovalent and bivalent cations, often with A being much larger than B, and X is a monovalent anion. The perovskite structure is named after the mineral $CaTiO_3$. This structure is generic and abundant, being found in many materials on and in earth.

When it comes to photovoltaic research, and optoelectronics in general, the vast majority of work in the past decade has looked at *organic-inorganic halide perovskites*. This class of perovskites places a large organic cation at the A-site, methylammonium (MA) and/or formamidinium (FA), a metal cation at the B-site, often lead (Pb) but possibly tin (Sn), and a halogen at the X site. These materials benefit a myriad features, including

- **Absorption:** due to their direct bandgap, organic-inorganic halide perovskites (OIHPs) have much higher absorption coefficients than their inorganic rival silicon, when it comes to higher-energy photons.

- **Thinness:** OIHP devices can therefore be thinner because of their high absorption; the can perform as well as 200 µm silicon devices while being nearly 1,000x thinner. Less material can therefore be used with no sacrifice made to efficiency.

fold here; this eases transportation costs, expands domains of use for it, and integration into structures and architecture. Additionally, flexible substrates allow for roll-to-roll device manufacturing.

- **Processing:** While silicon requires great pressures, high temperatures, and clean room environments to be successfully manufactured, OIHPs can be manufactured at room temperature, in normal lab environments, and, most importantly, can be entirely solution processed. These processes include spin-coating, doctor blading, and thermal evaporation. These techniques can be easily scaled for mass manufacturing; especially with flexible substrates, a factory may employ roll-to-roll manufacturing, so that layers of the PV can be added one-by-one as as large single roll makes its way through the factory, much in the manner photographic film and newspapers are currently manufactured.

- **Tunability** While the vast majority of work has been on methylammonium lead iodide ($MAPbI_3$, or MAPI), work has been done to replace ions in the A, B, and X locations. You can tune these sites for various reasons. A mixture of MA and FA might lead to higher stability; a replacement of lead for tin can ease environmental concerns; and mixing halogens leads to *bandgap tuning*, where one can vary the bandgap of the material from 1.6 eV (pure iodine), to 2.3 eV (pure bromine), all the way to 2.9 eV (pure chlorine). This extends optoelectronic applications to tandem solar cells, LEDs, and lasing.

As stated previously, much of the perovskite-related work here will focus on MAPI.

1.2 Bandgap Theory

As alluded to in Section 1.1.1, there is rich physics in solid-state theory. This section draws from several sources, including References [10], [11], and [1]. The reader is likely familiar with the quantum mechanical solution for a particle in a 1-D finite well, or a 1-D coulomb potential, where singular energy levels are spaced out, with forbidden regions of energy between them. If one then considers many wells, or many coulomb potentials, spaced out periodically, and plugs such a feature into Schrodinger's Equation, we obtain energy level splitting. This is shown graphically in Figure 1.4.

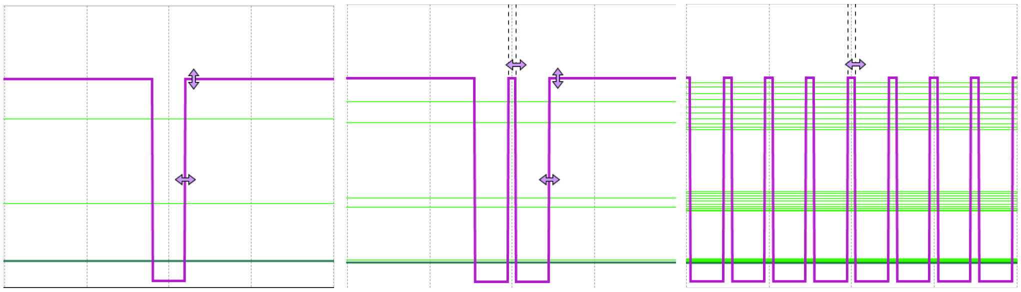

(a) One potential well **(b)** Two wells **(c)** Many wells

Figure 1.4: The splitting of energy levels as one adds potential wells. These results were obtained using the applet available at CU Boulder's PhET project.

With many potential wells, the allowed energy spectrum begins to form quasi-continuous bands of energy, with intraband energy spacing being on the order of 10^{-22}eV, while interband spacing, those regions of forbidden energy levels, is typically $10^2 - 10^4$meV.

This brings us to the distinction between a semiconductor, a conductor, and an insulator. The distinction exists solely due to Pauli's Exclusion Principle, which states that fermions may not share the same particle state. Therefore, as you "add" electrons to a system, they will have a tendency to first fill the lowest energy states, and following electrons will have no choice but to take the higher energy states. An analogy might be found in filling a glass with water; water will lower its energy state by occupying the $h = 0$ state, i.e. rest at the bottom of the cup. However, as the cup fills up, and the lower height states are occupied, the water molecules have no choice but to sit at higher heights. The highest state occupied by an electron is referred to as the fermi energy.

Conductors are then materials where the last highest energy state occupied by an electron exists in the middle of a energy band. This highest-energy electron has many intraband energy levels above it, and can freely move between energy states. However, if the highest occupied state is at the top of the energy band, with no available energy states directly above it, then this material is found to be insulating. One must overcome the interband gap in energy levels to kick an electron into a higher energy state. The highest occupied band of energy states is called the *valence band*, and the lowest unoccupied band is referred to as the *conduction band*. The forbidden energy zone between them is called the bandgap, and it is one of the most defining characteristics of a semiconducting material.

The distinction between semiconductors and insulators arises from the thermal distribution of electrons across their energy states, and can be seen in Figure 1.5. While the analogy of filling up a cup works for $T = 0$, but for $T > 0$, there is some non-zero probability that an electron occupies an energy above the fermi energy. This distribution in energy levels is referred to as a fermi-dirac distribution (Figure 1.5). The distribution, and the resulting carrier concentrations, can be seen in Figure 1.5.

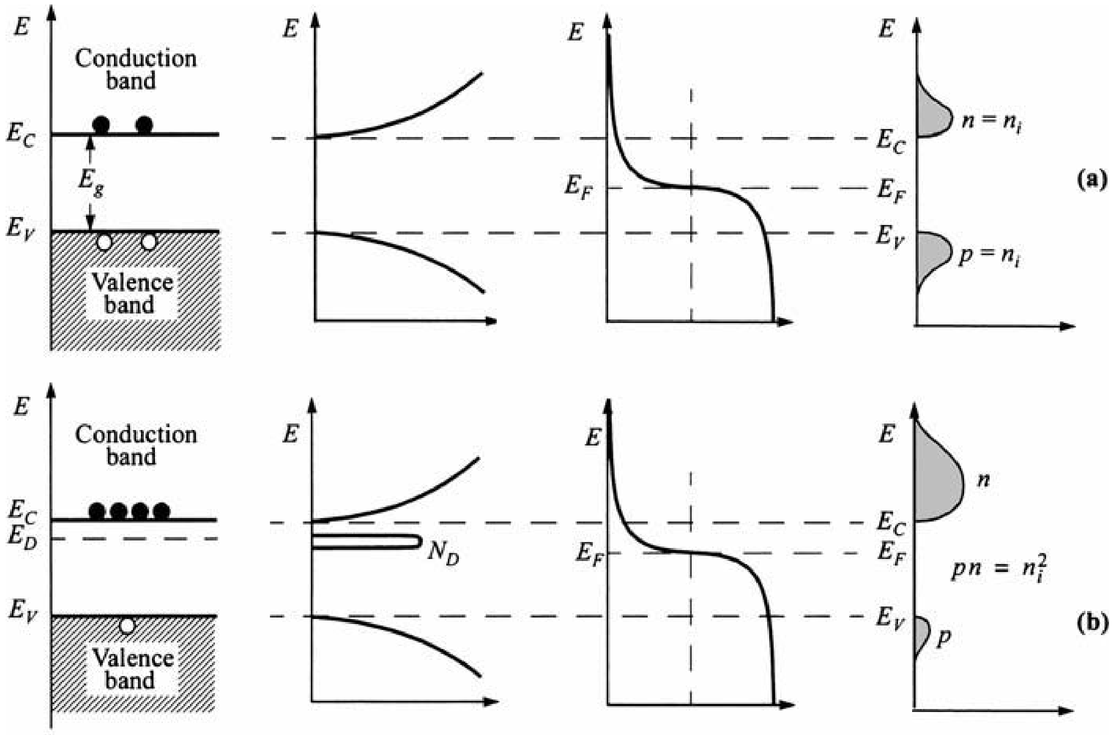

Figure 1.5: From left to right: a schematic of a semiconductor's energy bands, the density of states as a function of energy levels, the fermi-dirac distribution for $T > 0$, and finally the carrier concentration, which is a mathematical product of the fermi-dirac distribution and the density of states. The second row depicts the increase in electron carrier concentrations when the semiconductor is negatively doped. Adapted from Reference [1].

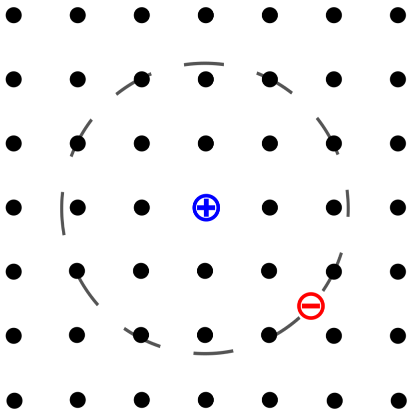

Figure 1.6: A bound electron-hole system, depicting the size of the exciton relative to the lattice spacing.

1.3 Quantum Dots

The theory of quantum dots is thus the result of of climbing up several orders of magnitude toward solid-state physics, learning about how a large collection of atoms behave, only to climb down a few rungs, but yet not quite so far down to where atomic theory lays. Typically, quantum dots are between 2 - 20 nm. However, scale is a necessary but not sufficient condition. A crystal that meets this size requirement is referred to as a *nanoparticle* or *nanocrystal*. A quantum dot has the additional feature of being of scale comparable to its *exciton bohr radius.*

The exciton bohr radius is analogous to the bohr radius of a hydrogen-like atom. Like the hydrogen atom, we have a single valence electron bound to a positive charge *via* the coulomb force. We can even estimate the exciton bohr radius using the traditional Equation 1.1, noting the change in permittivity and using the reduced effective mass of the electron:

$$a_{\text{exciton}} = \frac{\epsilon_r h^2}{\pi e^2 m_e^*} \tag{1.1}$$

Taking gallium arsenide as an example, with a permattivity of 12.4 ϵ_0 and a reduced effective mass of 0.025 m_e, has an effective bohr radius of about 24 nm! To compare, the largest-of-all-atoms cesium has a ground state radius of about a quarter of a nm and an excited bohr radius of 1 nm. One can see the enlarging effect being in a dielectric has on this bound state! An electron's orbit would not huddle closely to its central positive ion, but instead float many lattice points away, as seen in Figure 1.6. Such a classic solid-state physics result would have the orbit of the electron floating outside the walls of the crystal!

Quantum confinement's influence on the exciton's energy levels thus can not be ignored at these scales. Equation 1.2 shows the result for the energy eigenstates of a spherical infinite potential well:

$$E_{n,\ell} = z_{n,\ell}^2 \frac{\hbar^2 n^2}{2ma^2}, \tag{1.2}$$

where $z_{n,\ell}$ is a ℓth zero of the bessel function z_n, $\hbar$ is the reduced planck constant, m is the mass of the particle, and a is the radius of the sphere. It is in this respect quantum dots behave as physical manifestations of this classic system, with an inverse squared law relation to the radius of the well. However, some studies find best fits deviate from simple inverse-squared relationship between bandgap energy E_{bg} and particle size[12][2]. Reference [13] has a table summarizing the various fits groups have used for such data. Nonetheless, the bandgap energy of semiconducting quantum dots can then be easily tuned by engineering the size of QDs. Work by many groups, with many QD systems, have demonstrated bandgap engineering *via* size tuning [14]. Figure 1.7 summarizes some empirical work for PbS and PbSe QD systems.

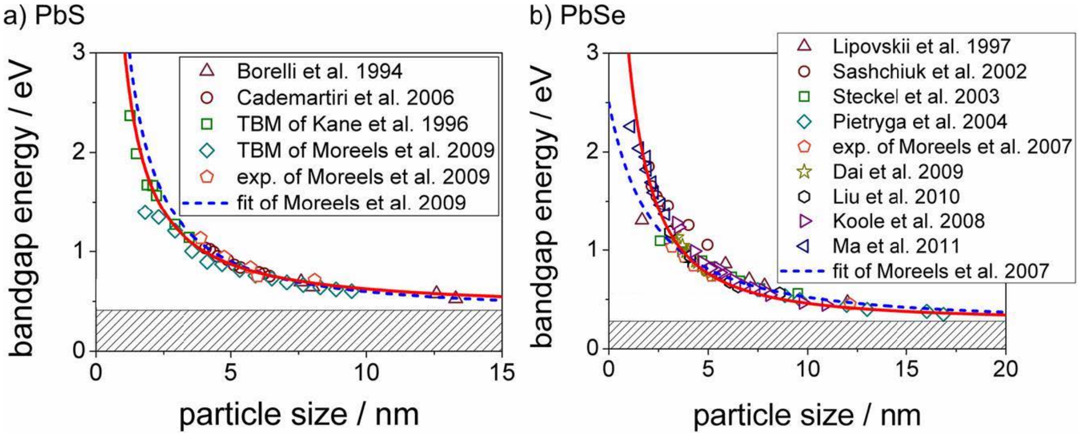

Figure 1.7: A plot of several group's mean particle size and respective bandgap. Adapted from Reference [2].

1.4 Device Physics Theory

Device physics, at least the parts of the field that we leverage, investigates how electric currents travel through the multiple layers and heterojunctions of electronic 'components'. Within this work, the components considered are optoelectronics, namely photodetectors, LEDs, and solar cells. Any of these components, or devices, are composed of several vertically-stacked thin films. For an LED, the charge carriers fight their way towards the so called ‘active’ layer of the device, where they meet, combine, and release a photon. A solar cell begins with charge carriers generated in the active layer through way of photon absorption, and through a combination of drift current and diffusion current, the charge carriers make their way to their respective electrodes to be carried out as electricity. In both cases, we want to choose a device architecture that enables our charge carriers to get where we want them to go.

Device architectures should have the valence band edges, conduction band edges, and work functions of the various materials working in concert to maximize current flow in the desired direction. While guided by the theory that follows, it is important to note that these simple models fail to predict the behavior of many metal-semiconductor heterojunctions. Particularly, surface states are known to cause deviations from prediction[15], and we can assume in “dirty” systems such as ours that our planar interfaces are riddled with such states.

As discussed above, due to the fact that electrons are fermions, every metal and semiconductor has a temperature-dependent distribution of occupied electron state. This distribution is dictated by fermi-dirac statistics (Figure 1.5, third column) and the density of states in a given energy range. The fermi energy E_f in

Figure 1.5 marks the energy level that has a 50% chance of being occupied. The energy required to bring an electron from the fermi level to vacuum is the work function.

When a metal makes "intimate" contact with a semiconductor, electrons will flow from the material with the higher fermi level to the material with the lower fermi level. This is simply due to lower energy levels now being available to the electrons, and is analagous to a container with a high water line being connected to a container with a low water line. Just like the water molecules in our analogy, the electrons in our two materials will move until there is a constant fermi level through the heterojunction. The resultant space charge (i.e. the electrons on one side and the holes they left behind on the other) leads to an electric field across the junction. This was first theorized by Schottky in 1938, which is in German, and by Mott that same year[15] [16]. The key metric in determining this distinction, according to the Schottky-Mott rule, is whether the semiconductor's or the metal's work function is larger. Critically, this field can be *rectifiying* or it can be *ohmic*, depending on which material has the larger fermi energy. As shown in Figure 1.8, the size of the rectifying barrier is proportional to the difference between the metal's work function and the metal's electron affinity.

However, in this line of work, it is important to note that the schottky-mott rule is an idealization. Often, unwanted contamination on the metal surface causes

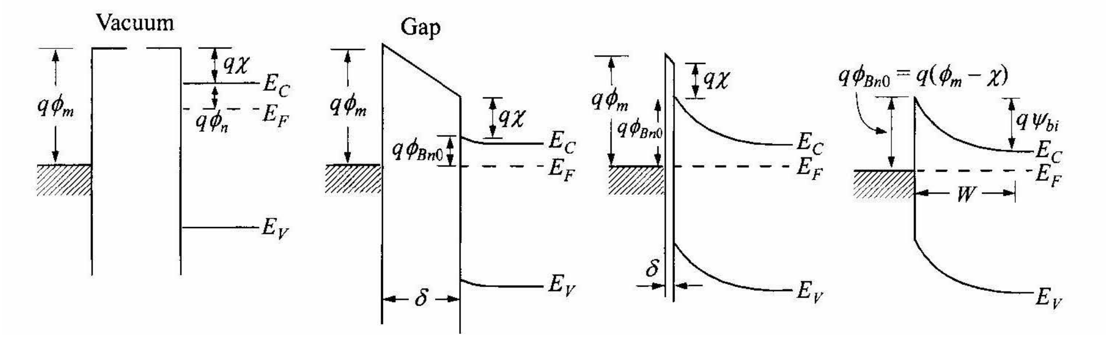

Figure 1.8: A metal-semiconductor junction. As the contact becomes intimate, electrons flow from the material with the smaller work function to the material with the larger work function. This results in an electric field at the interface. For $(\chi + \phi_n) < \phi_m$ (where χ is the semiconductor's electron affinity, ϕ_n is the energy difference between the conducting edge and the fermi energy, and ϕ_m is the metal's work function) the resulting space charge acts as a rectifying boundary. Adapted from chapter 3 of Sze's *Physics of Semiconducting Devices*Reference [15].

changes in a metal' work function Additionally, surface states on the semiconductor add unforeseen energy levels to the otherwise forbidden bandgap. It is therefore important to experimentally determine ideal ohmic contacts for a particular system. We use collected data, such as what is seen in Figure 1.9.

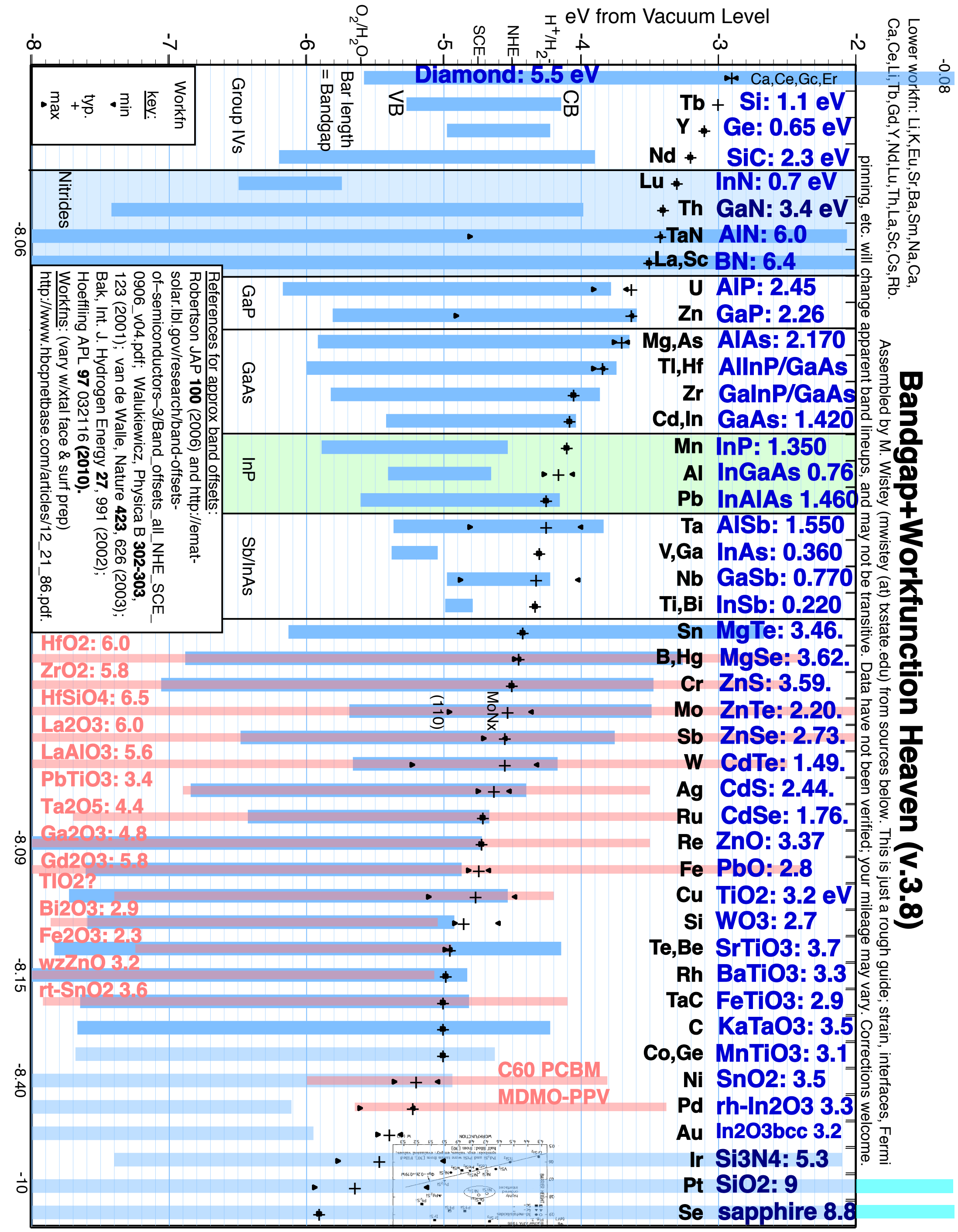

Assembled by M. Wistey (mwistey (at) txstate.edu) from sources below. This is just a rough guide; strain, interfaces, Fermi pinning, etc. will change apparent band lineups, and may not be transitive. Data have not been verified; your mileage may vary. Corrections welcome.

References for approx band offsets: Robertson JAP **100** (2006) and http://emat-solar.lbl.gov/research/band-offsets-of-semiconductors-3/Band_offsets_all_NHE_SCE_0906_v04.pdf; Walukiewicz, Physica B **302-303**, 123 (2001); van de Walle, Nature **423**, 626 (2003); Bak, Int. J. Hydrogen Energy **27**, 991 (2002); Hoeffling APL **97** 032116 **(2010)**. Workfns: (vary w/xtal face & surf prep) http://www.hbcpnetbase.com/articles/12_21_86.pdf.

Figure 1.9: "Bandgap Heaven", a compilation of conduction edges, valence edges, and work functions for various metals, semiconductors, and insulators. Device physicists often reference such documents for guidance on device architecture.

Chapter 2

Experimental Methods

There are two categories of experimental methods that are included in this chapter. The first section will focus on fabrication techniques, while the second section will focus on measurement techniques. Fabrication involves the creation of the optoelectronic devices focused on in this work. Measurement discusses the techniques used to assess a variety of properties of our materials and devices.

2.1 Fabrication Techniques

Traditional inorganic semiconductors, like germanium and silicon, cannot simply be dissolved in solution and then dried to reform crystallite structures. However, OIHPs, and the organic materials that make up their transport layers, can leverage their solubility and low formation energy to utilize these cheap highthroughput forms of film formation.

2.1.1 Spin-Coating

Far and away, the most common thin-film deposition technique used in my work is spin coating. As seen in Figure 2.1a, one begins by placing the substrate on a platform attached to a vacuum line. A solution with your dissolved material of choice is then deposited in the center of the substrate. Secured by the active vacuum, the spin coater can accelerate the substrate to a rotational speed of 1000s of RPM. This will result in the initial droplet spreading across the surface, a thin layer hugging the substrate *via* surface tension while excess solvent flies off. As it continues to spin, the solvent evaporates and what is left is the solute, which has hopefully self-organized into a compact layer[17]. Depending on the material, drying or annealing after spinning might promote better layer formation. The key parameters to investigate for successful spin coating includes molarity of solvent, spin coating speed, the vapor pressures of your solvent(s), and the ratio in which you might use solvents. It is often recommended that a combination of a high vapor pressure and a low vapor pressure allows for uniform, organized layer.

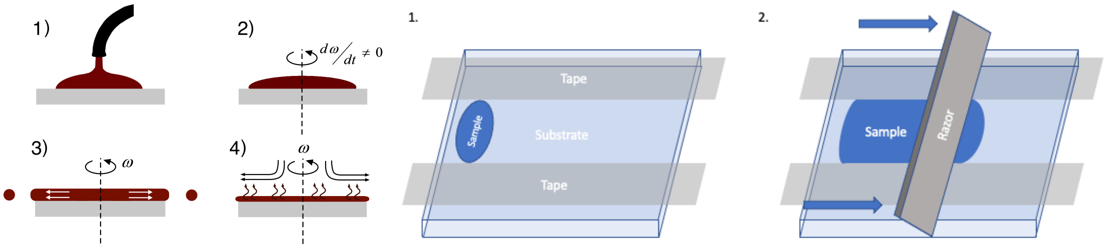

(a) Spin coating procedure **(b)** Doctorblading procedure

Figure 2.1: **a)** Spin coating steps, including a1) the deposition of a solution, a2) the initial acceleration of the platform, a3) when the platform reaches a steady-state speed ω and volume is lost due to centrifugal forces, and a4) where volume is now lost primarily through evaporation. **b)** Doctorblading, where one simply drags the sample in a crevice or well to form a layer to be dried.

2.1.2 Doctor Blading

Doctor blading is another way to easily form a layer of crystalline material. The mechanism is straightforward: you apply a mask of tape on either side your substrate, and deposit your solution or paste at the edge. You then use an edge, like a razor or squeegee, and drag the material across the substrate. The tape and substrate, acting together as a very thin well, hold a layer of the material uniformly across the substrate while the dragged edge scrapes the excess off. Figure 2.1b graphically illustrates this process.

For better or worse, doctor blading struggles to get layers as thin as spin-coating might; it is dependent on the make-shift channel formed by the tape. We apply our TiO_2 layers *via* doctor blading, which forms a 500 nm layer after sintering at 500 C for 45 minutes.

2.1.3 Thermal Evaporation

Thermal evaporation leverages the increased vapor pressure of metals at low pressures and high temperatures. Desired electric contacts are placed in tungsten boats, with a voltage applied across the boats to raise the temperature *via* ohmic heating. Pressures are then lowered to less than than 10^{-5} torr or about 10 billionth of atmospheric pressure, to allow for metal sublimation. Evaporation rates are controlled by the amount of current run through the tungsten boat. All the metal contacts found in this work (gold, silver, lithium fluoride, calcium, and aluminum) are deposited in this manner.

2.2 Characterization Techniques

2.2.1 Photoluminescence Spectroscopy

Photoluminescence spectroscopy (PL) is a direct way to measure to measure the bandgap of luminescent materials. Its operation is simple: a broadband light source is attenuated by a monochromator, such that a high energy wavelength of light is incident on a sample. Then, a detector sits elsewhere, measuring the photons coming from the surface of the sample. The detector monochromator steps through a range of wavelength values, measuring the quantity of secondary photons for each wavelength. Since most radiative emission occurs band-to-band,

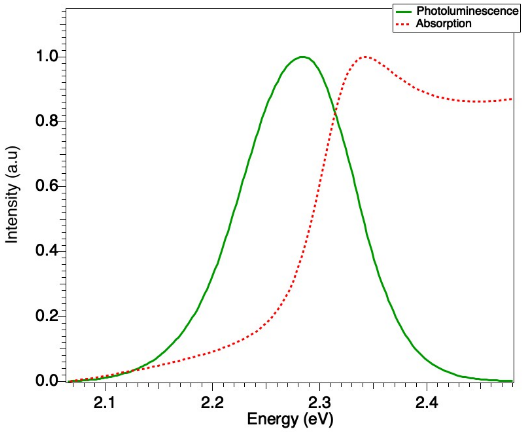

Figure 2.2: Normalized curves of both photoluminescence and absorbance for FAPbBr$_3$. As expected, the photoluminescence peak coincides with the absorption edge.

the peak of this emission profile tells us the size of the bandgap. Figure 2.2 shows the optical bandgap of FAPbBr$_3$ is approximately 2.28 eV. We use a Perkin-Elmer LS-45 spectrometer for PL measurements.

2.2.2 Absorption Spectroscopy

Absorption spectroscopy takes advantage of the fact that there are only 3 ways for incident light to interact with a sample: it may reflect off the surface, it may be transmitted through the sample, or it may be absorbed by the sample. For matte materials like ours that lack reflectivity, we use the simplified expression

$$1 = A + T \tag{2.1}$$

where A is the fraction of absorbed light and T is the amount of transmitted light. Here, absorption A is a property of thickness of a sample, and not a generalizable property of the material. The intensive property *absorbance* is the generalizable value that dictates how much absorption occurs per unit depth. Since transmission is what is measured in a spectrometer, absorbance α is defined as

$$\alpha = \log_{10}\left(\frac{1}{T}\right) = 2 - \log_{10}(\%T) \tag{2.2}$$

where $0 < T < 1$ and $0\% < \%T < 100\%$.

Like PL measurements, absorption spectrometers also go in the following order: light source, light monochromator, sample, detector monochromator, and detector. Here, the light is incident normal to the surface of the thin film. The distinction here is that the monochromators move in sync with one another, so that we are directly measuring how much of the source light ‘goes through’ the sample and makes it to the detector. This is measuring the transmission as a function of wavelength, $T(\lambda)$. If all the source light goes through, T = 1 (or 100%); if the light is completely absorbed, T = 0. As one would expect, photons with energy below the bandgap energy mostly will not be absorbed by the material. As the photon energy approaches the bandgap energy, absorption picks up. A normalized example of absorbance is shown in Figure 2.2. We use a Jasco V-670 spectrometer for absorbance measurements.

2.2.3 Atomic Force Microscopy

Atomic Force Microscopy (AFM) is a great way to measure the morphology of a surface. The importance of this cannot be disputed: rough surfaces lead to trap states between layers, and may cause pinholes in a layer that lead to electrical shorts.

All AFMs have an atomically sharp tip, which hangs from a cantilever, to measure its nanometer-scale distance from the surface. As the tip is brought nanoscopically close to the sample surface, electrostatic repulsion forces act on the tip. While conventional AFMs use a laser to measure the cantilever's deflection, the nGauge has a piezoresistive sensor attached to the tip. As the tip is moved along the area of the surface sample, the AFM measures strain and identifies changes in strain as changes in surface height.

Much device fabrication is guided by AFM results, finding what fabrication processes lead to smoother films. Surface roughness can be quantified within a measured area by a) defining a mean plane by averaging all pixel heights, and then b) determining the average difference between a pixel's height. For a profile of measurements of size m by n, this can be mathematically summarized as

$$R_{\text{avg}} = \frac{1}{mn} \sum_{i=1}^{m} \sum_{j=1}^{n} Z\left(x_i, y_j\right) - \mu \tag{2.3}$$

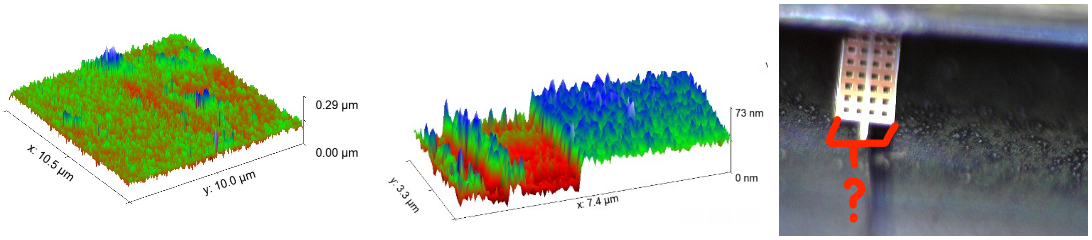

(a) **(b)** **(c)**

Figure 2.3: a) A 10µm x 10 µm AFM profile of $\mathrm{MAPbI_3}$ used to measure roughness. b) An AFM profile of a razor blade score on PEDOT:PSS. c) an optical photograph of the razor blade score on the surface of a sample.

where average height μ is

$$\mu = \frac{1}{mn} \sum_{i=1}^{m} \sum_{j=1}^{n} Z\left(x_i, y_j\right), \tag{2.4}$$

and Z is the height at pixel (x_i, y_j).

Besides roughness, the other sought-after parameter garnered from our AFM is a layer's thickness. AFMs cannot differentiate between layers, so measuring the thickness of a complete device is not useful. Instead, by applying a single material layer on a glass substrate, we can approximate that material's thickness when sandwiched into our device architecture. The layer thickness once in a device will deviate from this measurement, due to the fact that it is no longer being deposited on glass. We measure the thickness by scoring the material's surface with a razor. Using the AFM and an optical microscope, one can place the AFM tip on the edge of the score, and measure the height. Figures 2.3b and 2.3c depict this placement *via* optical microscope and a typical resulting measurement profile.

2.2.4 Current-Voltage Measurements

For current-voltage (IV, or JV for current density) measurements, we use a Keithley 2400 sourcemeter. This is a programmable current/voltage source and multimeter. I have programmed remote data acquisition software in Igor Pro to be used in conjunction with this sourcemeter. These Igor Pro programs can be found at `https://github.com/rsfadia/Igor-Pro-Data-Acquisition`.

Chapter 3

Simulation of Raman Spectrum for Germanium Quantum Dots

Note: some of this work was published in Reference [4]. However, much of it was revisited and updated during the writing of this chapter.

Raman spectroscopy (or Raman for short) is an indispensable measurement technique used to ‘fingerprint’ chemicals based on their vibrational modes. Whereas many optical measurements found in this thesis focus on the electronic modes of materials, Raman measures excitations of the molecular bonds in the material[1]. These excitations are vibrational modes in the sample, and the quantum mechanical treatment of these vibrational modes results in a quanta of vibration called a photon. The energy spacing between the excited states’ energy levels acts as a signature for a particular material, and allows us to identify what is in a sample.

Raman spectroscopy's main feature is a monochromatic excitation laser that is transmitted through the sample. To the human eye, these transmitted photons are unaltered by the sample. However, with a detector on the other side, we are able to detect the slightest shift in frequency. Photons interacting with molecules can be scattered elastically (rayleigh scattering) or inelastically (Raman scattering). Whereas rayleigh scattering releases a photon of the same energy, though in a random direction, Raman scattering describes a photon that has interacted with a phonon. This inelastically scattered photon will have exchanged energies with the impinged quasiparticle; almost always, it will have contributed some energy to the particle, resulting in a particle with a higher vibrational state and a photon with a lower energy; this loss of photon energy is called a stokes shift. Sometimes, one may have anti-stokes Raman scattering, where the photon interacts with an already excited molecule, and leaves the interaction with *more* energy than it started with. The energy diagram shown in Figure 3.1a shows a schematic illustrating both forms of inelastic scattering.

3.1 Background & Theory

The key distinction between Raman spectra for bulk and nanocrystalline materials lies in the relaxation of crystal momentum conservation. Take a typical

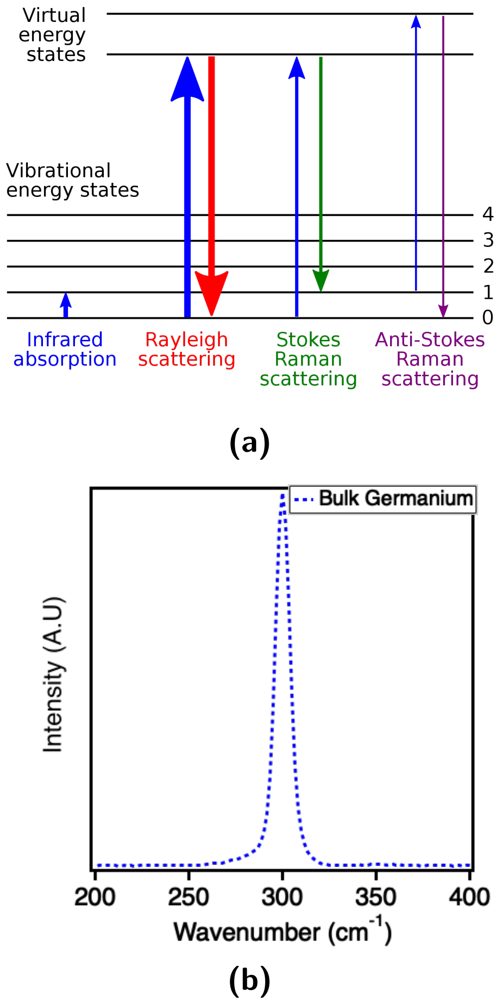

Figure 3.1: a) An energy-level diagram depicting rayleigh/elastic scattering and inelastic/Raman scattering. b) An experimentally acquired Raman spectrum for a bulk germanium wafer. Its peak sits at 301 cm^{-}1.

Raman setup, for example, where an infrared photon is incident on a sample, and backscatters towards the detector while creating a phonon mode in the sample. This is summarized in Equation 3.1 as

$$\vec{k_{\gamma i}} = \vec{k_{\gamma f}} + \vec{k}_{\text{phonon}} \tag{3.1}$$

With the scattered photon being measured behind the IR source, we may say $\Delta\theta = 180^o$. Since the change in wavelength is so small for the photon, we may approximate that $\vec{k_{\gamma i}} = -\vec{k_{\gamma f}}$. Therefore,

$$k_{\text{phonon}} = 2\vec{k_{\gamma}}. \tag{3.2}$$

As a typical example, let us assume our IR source has a wavelength of 1000 nm, so $2k_\gamma \approx 10^5\text{cm}^{-1}$. Compare this to the highest wavenumber optical phonon, found at the edge of the first brillouin zone, of value $k = 2\pi/a$, which is $\approx 10^8\text{cm}^{-1}$ for a typical lattice vector $a \approx 5\text{Å}$. We must conclude Raman spectroscopy, in order to obey crystal momentum conservation, can only investigate the inner 0.1% of the brillouin zone that sits about $k = 0$.

Since crystal momentum conservation is relaxed for nonperiodic structures, Raman spectra for amorphous and nanocrystalline material examines the whole phonon mode. With the breadth of the optical phonon mode available to spectroscopy, we get a broadening and general red shift due to the negative group velocity found about $k = 0$ (Figure 3.2). It should be noted that this confinement effect is not the only possible culprit for our broadened, red-shifted Raman

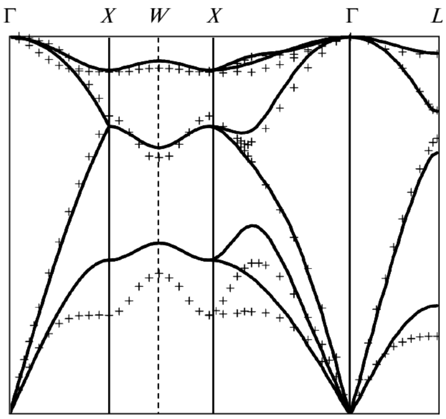

Figure 3.2: A figure depicting calculated (solid lines) and experimentally determined (markers) germanium dispersions. One can see at $k = 0$, represented by the Γ line, six phonon modes. There are three acoustic modes at the bottom, and three optical modes at the top. There is much degeneracy among these phonon groups, especially about Γ, though one can see the degeneracy break in the leftward phonon modes towards the X line. For all three optical modes, the negative slope about Γ predicts access to lower frequency modes and therefore a red shift in spectra once selection rules are relaxed. Figure adapted from Reference [3].

spectra; Paillard *et. al.* cites disorder from the amorphous or oxidized surface of the QD, as one contributor to spectral changes[21], Roodenko *et. al.* [19] try to account for lasing heat in their model, and Hesset *et. al.*[20] shows that strain on the QD's surface causes a peak shift.

The one phonon model, as it often called, was first fleshed out by Richter, Wang, and Ley in 1981[18]. They begin by modifying a typical phonon bloch wave of form

$$\psi = u(\vec{k}, \vec{r}) e^{-\vec{k} \cdot \vec{r}} \tag{3.3}$$

where $\hbar\vec{k}$ is the crystal momentum vector, $\vec{r}$ is the position, and u is some function modulating the plane wave that has a period equal to the lattice's period. This eigenstate, suitable for an infinte lattice, must be 'localized' by some weighting function to adequately reflect a phonon in a nanocrystal. This is generically written as[19]

$$\Psi = \psi \cdot W(\vec{r}). \tag{3.4}$$

The seminal Richter-Wang-Ley Model (RWLM) begins by defining a weighting function that serves to localize the phonon to the nanocrystal. Ricther *et. al.* define it to be a gaussian with standard deviation $L/2$, where L is the length of the nanocrystal. Using the full-width-half-maximum as a proxy for localization, they could then state that the phonon is confined to $\sqrt{\ln 2}L \approx 0.83L$. Other researchers have mostly followed in their stead with a normal distribution, such as Volodin[3] and Hessel[20] (though with varying standard deviations), and others still have used $\mathrm{sinc}(x)$[21] or square waves[19]. The work of Reference [19] does a particularly good job of summarizing the literature's array of choices for σ.

As described in today's literature, the next step in the RWL model, after having chosen a weighting function, is to mathematically describe the phonon dispersion. Before numerical methods were so readily available, papers like References[18] and [22] modeled silicon's optical phonon modes as one averaged cosine functions, as this mimicks well the isotropy and negative dispersion centered at the Γ point in Figure 3.2. However, as Paillard *et. al.* show in Reference [21], improvement can be made by accounting for anisotropy. Paillard *et. al.* utilizes Brout's Sum

Rule formulation to reduce the dispersion relations to some average dispersion relation

$$\bar{\omega}_0 = \sqrt{\frac{1}{3}\left(S(\vec{q} = 0) - \sum_{\text{acoustic}} \omega_i^2\right)}, \tag{3.5}$$

where $S(\vec{q} = 0)$ is the bulk peak frequency and ω_i are the phonon acoustic modes.

All this work describing the weighting function and the phonon dispersion are put together to solve for a Raman spectra. I note that the original Richter *et. al.* paper[18], though it shows a final calculated spectra in graphical form, does not explicitly state the calculation that provides said result, nor is a explicit dispersion relation given. The next pivotal paper in the literature, by Faucet and Campbell[22] in 1986, explicitly describes the calculation to be

$$I(\omega) = \int_0^1 q^2 dq \frac{\text{F.T.}\left[W(\vec{q}, r)\right]}{(\omega - \omega(\vec{q}))^2 + (\Gamma/2)^2} \tag{3.6}$$

where $\vec{q}$ is the normalized wave vector (in units of $\frac{2\pi}{a}$), ω is the bulk crystal's frequency, $\omega(\vec{q})$ is the analytic expression of the optical phonon dispersion, and Γ is the Full-Width-Half-Maximum (FWHM) of the bulk Raman peak. The integrand is the Fourier transform of the weighted wave function, as described in the previous paragraph, multiplied by a Lorentzian. More recent papers have added a Bose-Einstein term to this calculation to further weigh certain phonon modes, but such an addition did not impact our results.

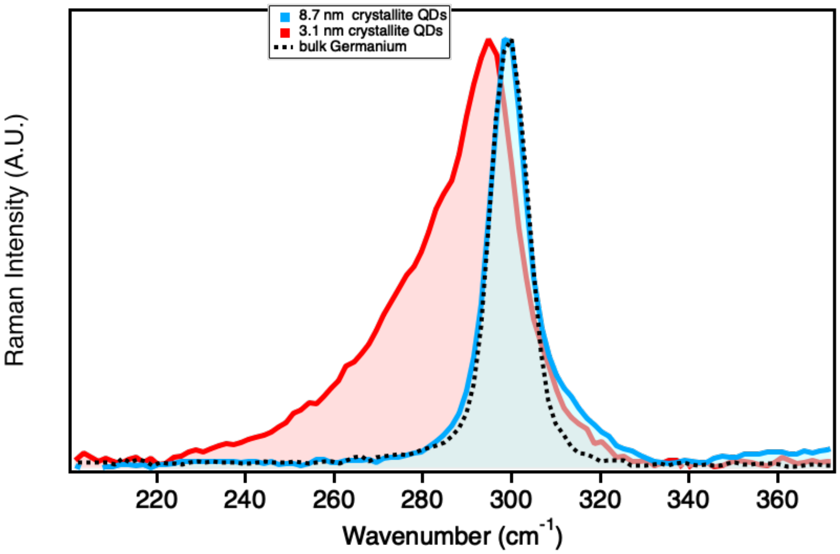

Figure 3.3: Bulk germanium (gray) sample compared to samples of large (blue) and small (red) quantum dots. As our dots get smaller, we get larger low-energy broadening. Initial high-energy broadening is likely due to strain between the crystalline core and the amorphous germanium shell. This is all collected data and not modeled.

3.2 Modeling Germanium Quantum Dots

My work explored understanding how to model the quantum dots fabricated by our collaborators at University of California, Davis. The synthesis of these dots is detailed in Reference [4]. The thesis of their work showed that one could tune nanocrystallite size by varying the doping of iodine or bromine in the synthesis process. Table 3.1 summarizes those results using germanium (IV) iodide, diatomic bromine or diatomic iodine.

We can see our particle sizes run the gamut of typical nanocrystalline sizes, the order of magnitude between 2 nm and 20 nm. Interestingly, as can be seen

	Crystallite sizes (nm)		
mmol	I_2	Br_2	GeI_4
0.00	3.1 ± 0.10	3.1± 0.10	3.1± 0.10
0.05	3.4 ± 0.10	3.3± 0.10	3.4± 0.10
0.10	4.0± 0.10	4.1± 0.10	4.7± 0.10
0.15	6.6± 0.10	4.7± 0.10	9.1± 0.10
0.20	8.7± 0.10	5.6± 0.10	11.7± 0.10
0.30	16.8± 0.20	8.7± 0.10	ND
0.40	17.7± 0.20	17± 0.20	ND

Table 3.1: Crystallite sizes for various precursor molarities.

in figure 3.3, confinement behavior dissipates by the times particles get 9 nm or larger. Yes, there is still asymmetric, high energy broadening for large dots due to strain between the shell of amorphous germanium and the crystalline core[20]. Meanwhile, the stokes shift and low-k broadening seen for the 3.1 nm crystallites is due to the relaxation of selection rules for small crystallites, and it is apparent in figure 3.3 that even 9 nm QDs are large enough to be excluded from such effects. Note how form-fitting the 8.7 nm line is to the bulk germanium Raman spectrum after the onset of the signal.

When trying to model Raman spectra, there are many parameters to consider:

1. what phonon dispersion should one use?

2. what weighting function should one use?

3. with so many choices in the literature, what variance does one use in the weighting function?

4. is a phonon confined to the inner crystallite, of size extrapolated from XRD *via* the Scherrer equation, or the total nanoparticle size, as measured by electron microscopy?

5. does one assume that there is size distribution that makes a meaningful difference?

6. if one assumes a size distribution, what does that distribution look like?

Some of these details are examined closely in this work. Others, we must just assume.

To start with, we use an average phonon dispersion calculated by Paillard *et. al.* in his work studying germanium quantum dots encased in silicon oxide. Using their Brout sum method, a method successfully used in earlier work [21] for silicon QDs, they find the phonon dispersion to be

$$\omega(\vec{q}) = \sqrt{301^2 - \frac{43565\, q^2}{|q| + 0.5766}}, \tag{3.7}$$

where q is the reduced phonon wave vector that is valued from 0 to 1 across the first brillouin zone. This fit forms well to the optical phonon modes found in germanium, as seen in the last section in Figure 3.2.

In line with most research, we use a normal distribution for the weighting function, as the literature has suggested the difference to be minute[19]. We then investigate the use of many possible variances. References [19] and [23] summarize some common values for variance σ^2, namely $\frac{d^2}{4}$, $\frac{d^2}{12}$, $\frac{d^2}{79.38}$, and $\frac{d^2}{16\pi^2}$, where d is the diameter of the particle. This variance is used in the weight function and its corresponding Fourier transform:

$$W(\vec{r}) \propto \exp\left[-\frac{\vec{r}^2}{2\sigma^2}\right] \text{ and F.T.}\,[W(\vec{r})] \propto \exp\left[-0.5\vec{q}^2\sigma^2\right] \tag{3.8}$$

Throughout this work, we ignore coefficients, including those belonging to the expressions above, as all simulated spectra are ultimately normalized to be compared to likewise normalized data. A smaller variance correlates to a more confined particle, and therefore one should expect an increased red shift.

Indeed, we see this expected shift in Figures 3.4. These plots calculate the Raman spectra for quantum dots of (average) size 3.1 nm and 8.7 nm. In both cases, we see the same pattern of increasing red shift for a smaller variance σ^2. Most interesting is how these two sets of models occupy two different limits; the two smallest variances (red and yellow) in the smallest dots do not differ measurably in the spectra. Meanwhile, we see the results between the two largest variances, $\sigma^2 = d^2/12$ (green) and $\sigma^2 = d^2/4$ (purple) is small for our largest dots. They are both narrow emissions, with a Δk of about 3 cm^{-1}. In both the small dot and large dot samples, their Raman specta are best fit by using a weighting function with the largest variance $\sigma = d^2/4$. We especially see a good fit for the larger samples. This makes sense since the larger dots deviate from bulk spectra less, and might be not test the limits of the RWL model. Unsurprisingly, things are hairier for the smaller dots. While it gets the peak of the spectra mostly right, it clearly overestimates spectra near the peak and underestimates emission for lower k.

Part of this poor estimation might be due to the limitations of the RWL model. In the original paper, Richter *et. al.* did not consider the effect of having a size distribution. However, we know that with a large size distribution, our spectra should shift a fraction of its area towards lower energy phonons, as we would have a larger fraction of the sampled dots be of small size. Larger dots do not cause broadening in the blue direction, so a wider size distribution always gives a net red shift and increased 'red' broadening. We see this discrepancy at play in Figure 3.4a, suggesting that there is a considerable size distribution. We thus take some time exploring how to implement a size distribution. Mathematically, this distribution is implemented by integrating the results of Equation 3.6 over particle size space.

$$I(\omega, \bar{d}, \sigma_d) = \int_a^b D(\bar{d}, \sigma_d) \left[\int_0^1 q^2 dq \frac{\text{F.T.}\left[W(\vec{q}, r)\right]}{(\omega - \omega(\vec{q}))^2 + (\Gamma/2)^2} \right] \tag{3.9}$$

where the new symbols represent some size distribution $D(\bar{d}, \sigma)$, some average size $\bar{d}$, and some variance σ_d^2

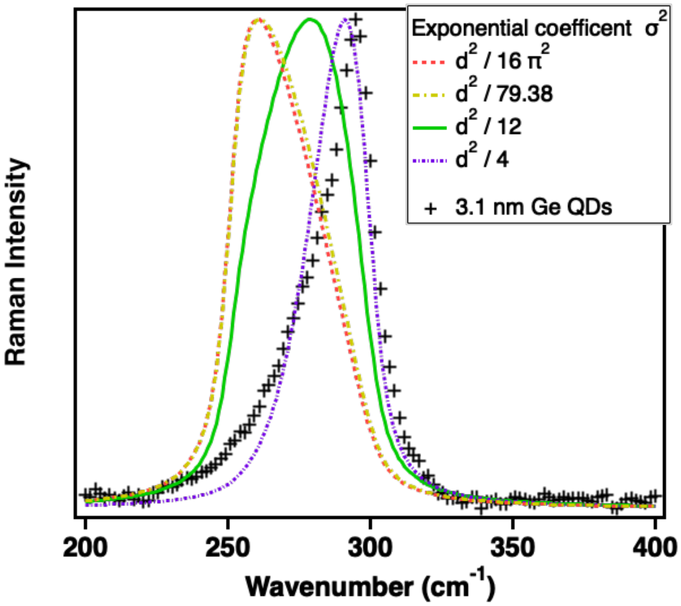

(a) 3.1 nm models (lines) and 3.1 nm data (crosses)

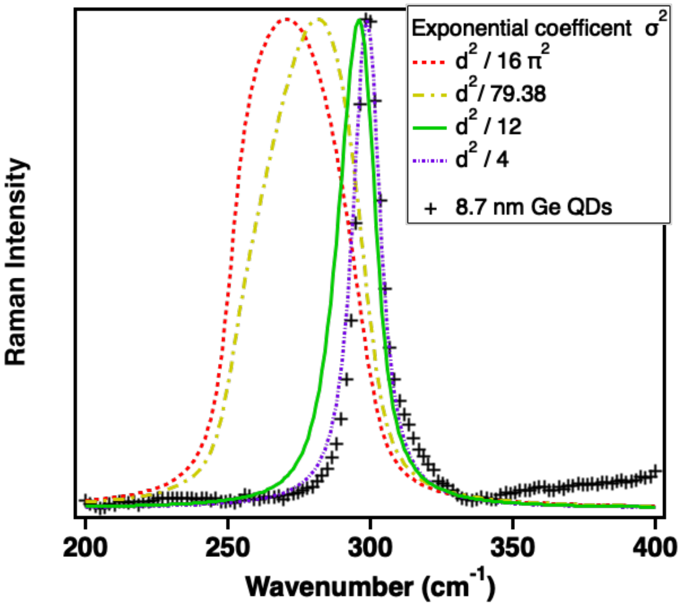

(b) 8.7 nm models (lines) and 8.7 nm data (crosses)

Figure 3.4: Two plots inspecting various variances for the weighting function $W(\vec{q},\vec{r}) = \exp\left[-\vec{r}^2/(2\sigma^2)\right]$ for dots of average crystallite size a) 3.1 nm and b) 8.7 nm. These dots were synthesized using an iodine precursor as described in Reference [4]. These calculations do not consider size distributions. These were calculated Using Equation 3.6.

Choosing what the size distribution was tough and not obvious. While in the future, measuring a histogram of size distributions will be the best strategy, we did not have such data available to us. What first came to mind is a gaussian distribution. Gaussian distributions have a clear average, and a clear standard deviation, both of which we have derived from electron microscopy results. However, gaussians suffer from not being strictly positive, and with a mean of 3 nm and standard deviations of 1.0 nm, a portion of the normal distribution will exist at zero or less nanometers. This is clearly unphysical.

Looking for a distribution that is strictly positive and "normal-like", I found the log-normal curve, which is defined as

$$P(x) = \frac{1}{S\sqrt{2\pi x}} \exp\left[-\left(\frac{\ln x - M}{S\sqrt{2}}\right)^2\right] \tag{3.10}$$

where M and S are the mean and standard deviation of the *log* of the distribution. We map between M,S, and the mean and standard deviation of the actual distribution μ and σ via

$$M = \ln\mu - 0.5\,S^2 \qquad \text{and} \qquad S = \sqrt{\ln\left[1 + \frac{\sigma^2}{\mu^2}\right]}.$$

For our work, if I wanted a log-normal size distribution with $\mu = 3.1$ and $\sigma = 0.8$nm, I would plug in $M = 1.099$ and $S = 0.2539$. Figure 3.5 graphs both distribution functions for our smallest average particle size of 3.1 nm and standard deviation 0.8 nm. Equipped with a function that predicts zero particles with size

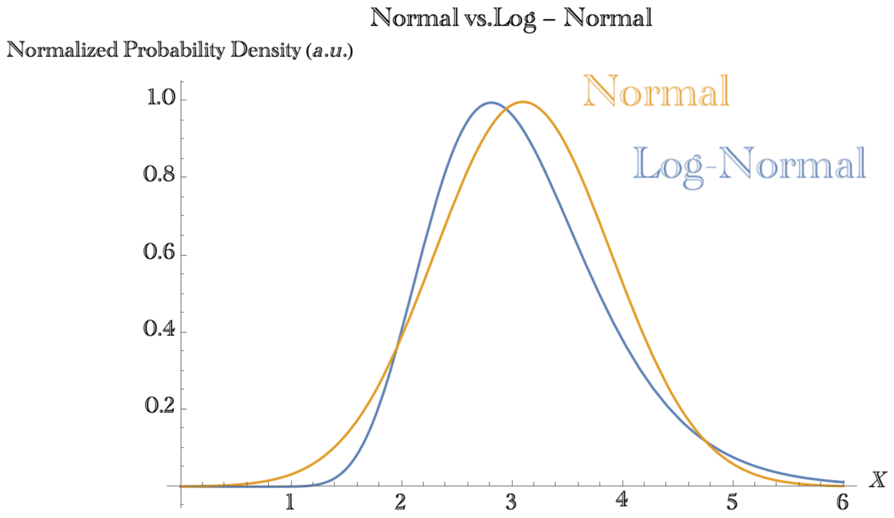

Figure 3.5: Graph showing the difference between a log-normal and a normal distribution given the same population mean and variance. Here, $\mu = 3.1$ and $\sigma = 0.8$.

$D = 0$, we can now confidently integrate size-space using Equation 3.9. No appreciable contribution to a spectra is made after $D = 10$nm for our variances, so that marks our upper bound. $D = 0$ is our lower bound. We can now re-do our work considering size distribution. It is important to note that this tail is exclusively a feature of a size distribution, and no combination of varying average particle size, standard deviations, or weighting function can result in such an asymmetric tailing as seen in 3.1 nm crystallite size found in Figure 3.4a, if one is assuming a singular particle size. However, once a particle size distribution is assumed, a solution is not unique. My work has found a few distribution functions that fit this data nicely. As mentioned above, it is unclear whether one should use the size of the crystalline core, as determined by XRD, or the nanoparticle size as determined by TEM. I note that work such as Reference [24] use the whole particle size, and not the crystalline core's size. Indeed, using an average size of 3.1 nm gets us results that skew quite far from the collected data; this is true for any relevant standard deviatoins used. However, when I assumed the particles were 4.7 nm in size, as TEM told us, a standard deviation of 1.3-1.7 nm explains this asymmetric tailing. Which value we use within that range depends on if one uses a normal distribution or log-normal distribution. These results are shown in Figure 3.6 However, it should be noted that our actual size distribution might not follow either of these distributions neatly, nor should we expect them too. However, by exploring two mathematical functions describing how our particle sizes may vary, we gain insight into how successful a synthesis process might be at creating quantum dots with narrow size distirbution, which is generally regarded to be a goal.

Future work should focus on extending beyond the Brout sum estimation. While it works well in practice, if we could fit equations to the actual phonon dispersion modes that are mapped out by neutron scattering, we might find a better, more generalized approach. The work of Volodin et. al. in Reference [3] begins to explore that, but without the use of size dispersions. As we saw here, considering a size distribution was the key to understanding why our Raman spectra was so asymmetrically broadened.

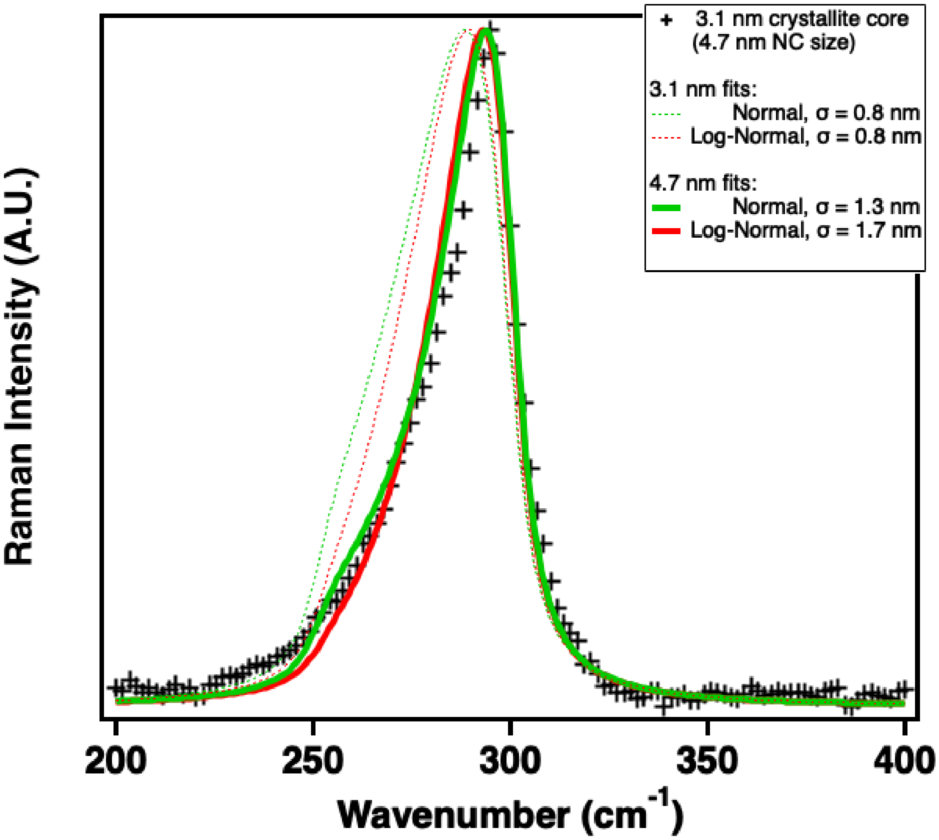

Figure 3.6: Raman spectra (black crosses) and models with varied parametes. All models use the same weighting function and weighting function variance. However, they vary in the implementation of the size distribution. The light, dashed lines show fits when we consider the XRD results, which suggest fitting to 3.1 nm. The solid lines

Chapter 4

Ge QD photodetectors

4.1 Background

Germanium is well known in the history of semiconductors: the first operational point-contact transistor was made by John Bardeen, Walter Brattain and William Shockley on the eve of Christmas Eve 1947. Despite its early market lead, and its natural upper hand in efficiency due to its lower bandgap and higher mobilities[**?**], germanium technology could not compete with silicon's natural abundance. While germanium transistors have fallen to the wayside, germanium technology is not obsolete. As a photodetector, germanium's smaller 0.7 eV bandgap allows for measurements much farther into the infrared spectrum ($\lambda_{\max} \approx 1800$ nm) than its silicon counterpart ($\lambda_{\max} \approx 1100$ nm). However, fabricating traditional germanium electronics-grade wafers is as energetically taxing as silicon, requiring high temperatures, pressures, and cleanrooms. Germanium nanoparticles can circumvent this issue, allowing for a cheaper solution-processed device fabrication route[25].

Here, we investigate the use of high-quality, monocrystalline germanium quantum dots (Ge QDs) in a thin-film photodetector architecture, using QDs synthesized by the Kauzlarich group in the chemistry department at the University of California, Davis. Their novel synthesis route leads to mono-crystalline nanoparticles with low size dispersion [5], as can be seen in figure 4.1, an improvement over previous results[26][27]. Previous work done in collaboration with our group and the Kauzlarich group found that the Ge QDs certainly have a photoresponse, but lack in power output[28]. For this reason, we explore optoelectronic devices that need no power output, namely photodetectors.

4.2 Experimental Methods

Zheng Ju, our Davis collaborator, synthesized three sets of Ge QDs: the first two sets, single-crystalline Ge QDs synthesized by the novel process being explored in [5], had average dispersions 10 nm and 18 nm. The third set was also 10 nm, but was prepared by a previously published method that results in less crystalline nanoparticles. This is summarized in Table 4.1.

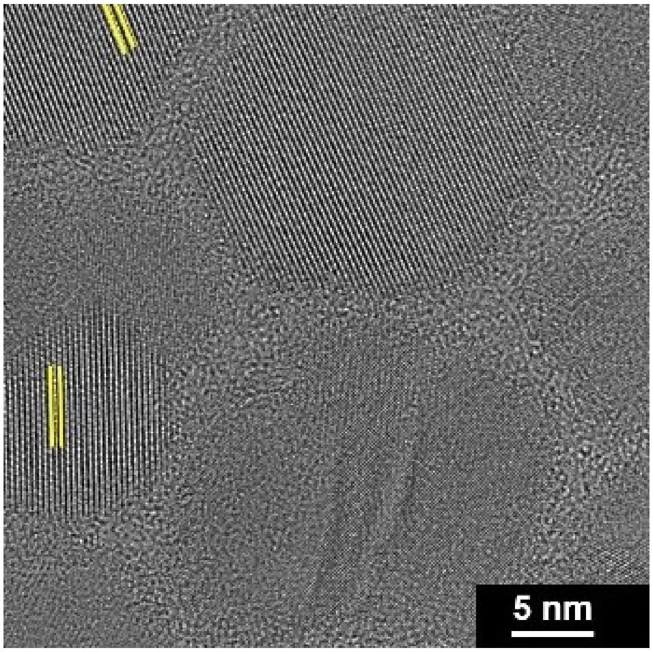

Figure 4.1: High-resolution tunneling electron microscopy images of highly-crystalline germanium nanocrystals, fabricated by Ju et. al. *via* novel two-step synthesis method. Adopted from from [5].

Sample	Particle Size	Crystallite Size
Poly-Crystalline QDs	10 nm	4 nm
Small Monocrystalline QDs	10 nm	7 nm
Large Monocrystalline QDs	18 nm	15 nm

Table 4.1: The three samples being investigated in this work. Whereas the monocrystalline samples have crystallite sizes comparable to their particle size, the polycrystalline dots' have a discrepancy between particle size and crystallite size.

To investigate how crystallinity of the nanoparticles impacts device performance, we fabricated photodetectors using the single-crystalline 10 nm Ge QDs (s.c. 10 nm QDs) and the poly-crystalline 10 nm QDs (p.c. 10 nm). Our best-performing device architecture is seen in figure 4.2. Indium tin oxide (ITO) serves as our anode. Following that, we have two TiO_2 layers. The first is the compact TiO_2 (c-TiO_2), whose valence and conduction bands to selectively transport photogenerated electrons to our anode. Atop that, there is a mesoporous TiO_2 (m-TiO_2) layer that increases the surface area with the perovskite absorption layer, increasing charge extraction. Collectively, the TiO_2 aid in electron extraction and hole blocking. While compact-TiO_2-only devices have been effective, having an additional mesoporous layer allows for further charge extraction from the absorption layer by way of increased surface contact. Patterned silver contacts, thermally evaporated on the active layer, served as our anodes. Light and dark measurements were taken using a Keithley 2400 sourcemeter, and a 6255 xenon arc lamp supplied by Newport Inc. White light incident on devices during light measurements was tuned to be 100 milliwatts/cm^2.

Tauc plots were also made to estimate the bandgap of these various QDs. This was done via photothermal deflection spectroscopy (PDS). These samples were on glass substrates washed, like the ITO slides above, by hand with detergent, followed by acetone and IPA sonication baths for 15 minutes each. The QDs were

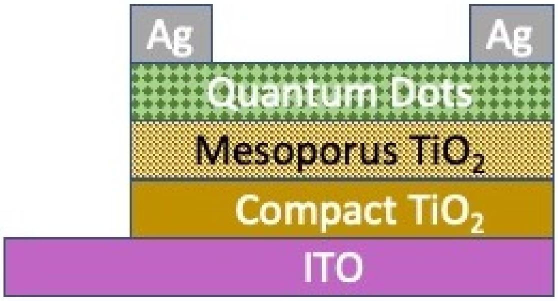

Figure 4.2: Device architecture of our germanium quantum dot photodetectors

dispersed in toluene, and were spin-coated between 400-800 RPM. Due to the nature of the synthesis method, batches of QDs had various concentrations and thus had to have spins tuned for a specific batch.

4.3 Results

4.3.1 Bandgap Estimates

Absorption data is presented in Fig 4.3. The inset shows that the s.c. and p.c. 10 nm crystals, despite being the same particle size, have differing bandgap size. This discrepancy can be explained by their differing crystallite sizes. While it is well known[25] that quantum dots have an inverse relationship between size and their bandgap, these results suggest that the crystallite size influences the resulting quantum confinement effects. The combined XRD and STEM data suggest two possible scenarios: the less crystalline sample might have a small

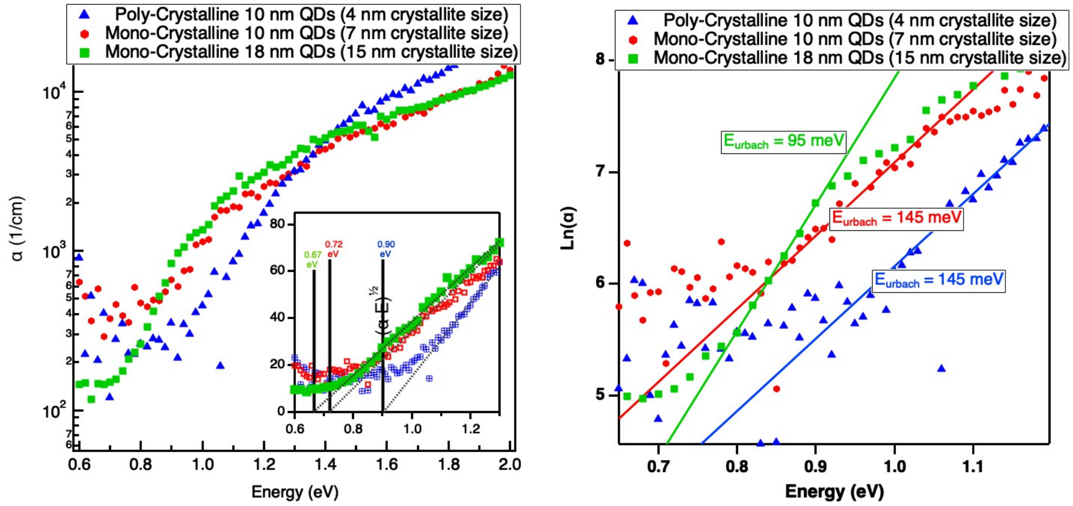

Figure 4.3: Left: Photothermal deflection spectroscopy of various quantum dot sizes. Listed are particle size, as determined by HAADF-STEM, and their corresponding crystallite size, as determined by fits to XRD results. Right: Urbach energy values, calculated *via* the reciprocal of the slope the intermediary linear region on a plot of log(α) *vs* $h\nu$.

crystalline core and an amorphous Ge shell, or it might have that shell as well as a polycrystalline core. Both interpretations would constrict the size of an exciton created by photo-absorption, leading to increased quantum confinement effects, which would explain the higher bandgap measured in the tauc plot inset in Fig 4.3.

4.3.2 Urbach Energy Estimates

Urbach energies were measured, with fits shown in the right panel of 4.3. Interestingly, disorder did not correlate with the quantum dot crystallinity, but instead the size of the dots; the monocrystalline and polycrystalline dots shared an Urbach energy of 145 meV, whereas our 18 nm dots had Urbach energies of 95 nm. This is not surprising if one considers the distinction of surface states from bulk states. Whereas surface states scale R^2, bulk states scale R^3, so larger dots benefit from a higher ratio of bulk states to surface states. The bulk of the dots is composed of germainum-germanium bonds; however, on the surface of a dot, are messy attachments of oleylamine ligands. Oxidation also may occur between the ligand and germanium nanocrystal, though oxygen contamination is not known to have occurred.

Chapter 5

Thickness Study of Hole Transport Layer in Planar $MAPbI_3$ Solar Cell

The reasons to study $MAPbI_3$ solar cells is obvious: their flexible architecture can lead to roll-to-roll production, which would be a dramatic improvement in fabrication costs over conventional solar cells; this could lead to a cheapening of cost per watt of available power. Additionally, silicon may be combined with perovskite for a tandem cell with improved efficiency.

For these reasons, our work was motivated to study device architectures that enabled such cheap and scalable processing. Therefore, the more classic n-i-p architecture using ITO/TiO_2/$MAPbI_3$/HTL/Au (where HTL is some organic hole transport layer) was discarded for an architecture with all-organic transport layers. This all-organic p-i-n archtecture (commonly referred to as reverse architecture) has several benefits [29]. Firstly, this does away with the 450 C sintering step required of the titanium dioxide layer. Secondly, electron collecting metallic electrodes, such as silver or aluminum, are much cheaper than the standard gold electrode used for n-i-p devices. Thirdly, organic transport layers are deposited considerably thinner than their inorganic counterparts, enabling their use on flexible substrates.

For this study, we studied the effects of various dilutions of this pre-dissolved PEDOT:PSS (or PEDOT for short). Our samples were some ratio of deionized H_2O to PEDOT. In this work, I will refer to samples by this ratio (e.g. 2:1 will mean two parts H_2O were added for every 1 part PEDOT). Alternatively, this 2:1 may be mentioned as a "200% dilution". Referring to the samples by dilution and not thickness is because we can not reliably measure such thin layers on our atomic force microscope. Approximations could be made, assuming a linear relationship, but I am unaware how accurate such an approximation may be.

5.1 Device Architecture

5.1.1 Layer Motivation

Many, many device architectures have been explored in the past decade [30]. Several have used the architecture used in this work [31, 32, 33], namely ITO/ PEDOT:PSS/ $MAPbI_3$/ PCBM/ LiF-Ag. This architecture and the associated energy levels are found in Figure 5.1. Indium tin oxide (ITO) is an oft-used transparent conductor used today in thin-film device research, and OLED and LCD screens. ITO-patterned glass substrates are purchased from Thin Film Devices, LTD.

Poly(3,4-ethylenedioxythiophene) polystyrene sulfonate (PEDOT:PSS) sits atop the ITO, semi-transparent conducting polymer used here as a hole transport layer. Its large work function also functions as an electron blocking layer, decreasing chances of recombination.

On the other side of the perovskite absorption layer is the electron collector layers. First, we have Phenyl C_{61} butyric acid methyl ester (PCBM). PCBM is composed of C_{60} molecules (commonly referred to as buckeyballs) bonded to an organic molecule. Studied for decades as a potential organic solar cell material, it is prized for its electron transport abilities as well as its solubility. PCBM's energy levels depend on preparation and measurement technique; the HOMO level, which

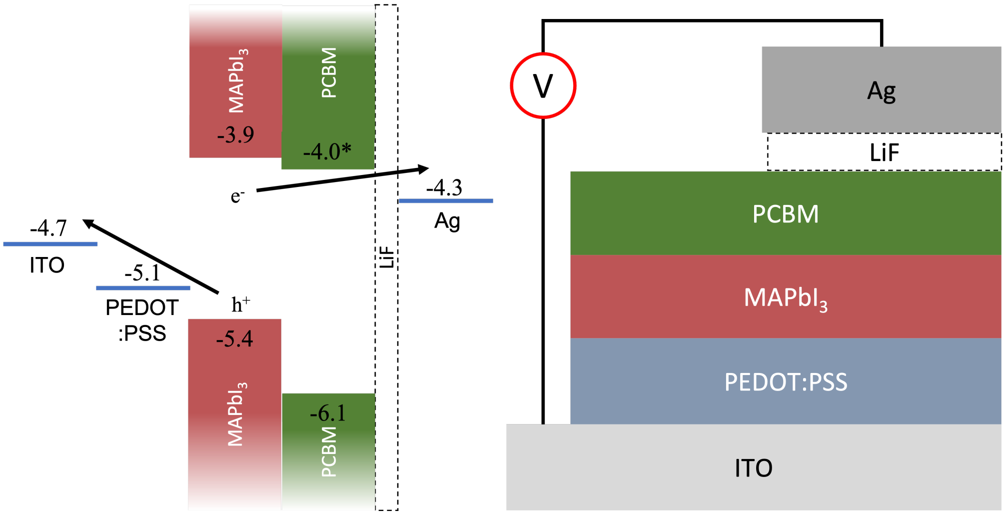

(a) **(b)**

Figure 5.1: a) energy level diagram for our perovskite solar cell. While hole transport layers have well documented work functions, the LUMO level of PCBM is disputed. Polycrystalline Ag has a work function of 4.3 eV, but a thin layer of LiF forms a dipole moment that benefits device performance. b) The device architecture in planar form. Thicknesses are not to scale.

is the more relevant band edge for our device, is reported with values between -3.8 to -4.2 eV. I use the mean of these reported values in Figure 5.1a.

Lastly, we add a back metal anode. Research into use of a thin buffer layer goes back decades [34, 35, 36] in use with other thin-film organic optoelectronics. It has been shown that such a buffer layer, like a 1-5 nm layer of lithium fluoride between your anode and electron transport layer, can benefit a device. Amongst other, some proposed mechanisms for this improved transport includes dipole-induced gap states and fermi level pinning[36, 34]. Reference [34] finds that the work function of Ag, Al, and Au are all pinned to 4.3 nm by a 5 nm layer of LiF.

5.1.2 Device Fabrication

The pre-patterned ITO was on a 1 in^2 glass substrate, with a 20 Ω/sq resistance at 150 nm thick. Unused substrates were cleaned initially by a vigorous scrub using alconox cleaning detergent and water. This was followed up with two 15 minute ultrasonication baths of acetone and IPA. Because all our layers are soluble, ITO substrates were washed and reused. The removal of the past device was *via* repeated q-tip scrubbing of deionized H_2O and ethanol. Then, the substrates were placed in sequential ultrasonication baths of detergent and DI H_2O. This was followed by the cleaning procedure above, with the bath times changed to 60 minutes.

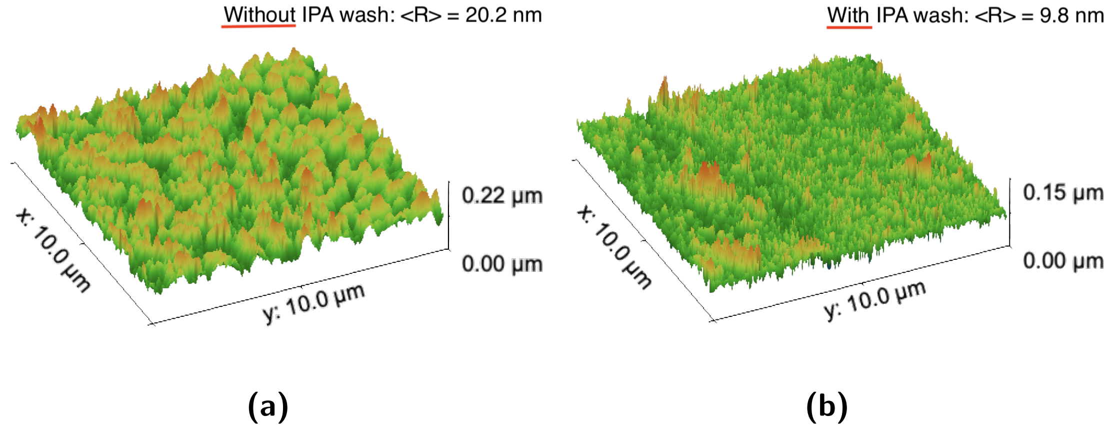

Figure 5.2: Atomic force microscope measurements of area A 10 µm x 10 µm for (a) two-step $MAPbI_3$ layer without an IPA wash, b) a similarly prepared $MAPbI_3$ layer with an IPA wash. Mean roughness measurements indicate that the IPA wash halves the surface roughness, decreasing trap states that would be found at the $MAPbI_3$/PCBM interface.

H_2O-dispersed PEDOT:PSS was purchased from Sigma Aldrich (product no. 655201). Any PEDOT solution is kept in a chemical refrigerator, and was always placed back in the refrigerator between substrate depositions. This was done to prevent any thermalization, which while not detrimental to the PEDOT:PSS, could affect its viscosity and thus spin dynamics. Cleaned substrates were prepared for PEDOT:PSS depositon by taping over the patterned ITO anodes, to prevent shorts or leakage current. Then, 130 µL of PEDOT:PSS was deposited in the untaped channel, sitting atop the patterned ITO cathode. This deposition had a 2 minute holding time before being spun at 4000 RPM for 60 s.

$MAPbI_3$ layer was deposited *via* a two-step deposition method. First, 25 µL 1M PbI_2 (Sigma Aldrich, 900168) in DMF is spin coated at 4000 RPM atop the

PEDOT:PSS for 30s. Immediately after the the PbI_2 spin stops, 200 µL 40 mg/mL MAI (901434) dissolved in IPA is laid atop the PbI_2 and held there for 25 seconds before initiating a 30 s spin at 4000 RPM. Before the MAI spin even begins, one should notice the yellow PbI_2 fading to a light brown, indicating perovskite formation. Once the spin is completed, the bright yellow PbI_2 has been replaced with a light brown $MAPbI_3$ layer that still has DMF solvent within its crystal lattice. We then place it on a hot plate pre-heated to 100 C and anneal for 30 minutes. Just a minute into this annealing process, the light brown layer should be visibly darker and matte, indicative of successful $MAPbI_3$ formation. After the annealing process is complete, 200 µL of IPA is deposited on the perovskite layer and spun for 30 s at 4000 RPM.

Once the IPA wash is completed, we deposit 18 µL of 20 mg/mL PCBM dissolved in chlorobenzene atop the perovskite layer. It is spun at 3500 RPM for 60 s. I then place the substrate on the 100 C hot plate to dry for two minutes.

The final step is a thermal evaporation of our cathode. 3-5 crystals of lithium fluoride were placed on a tungsten boat placed in a Kurt J. Lesker thermal evaporation system. Due to the extremely thin desired film thickness, it is appropriate to strive for as symmetric of an evaporation geometry as possible. I had best success when placing the lithium fluoride in the middle boat, directly beneath the substrate mask. Power across the LiF's tungsten boat was slowly increased, in order to achieve (to varying success) a deposition rate no greater than 0.2-0.3 Å/s. Current across the boat was cut at 1.0 nm. Silver was placed in the left tungsten boat, acknowledging that the devices would likely not suffer from a varying silver thickness so long as it is sufficiently thick. A 70-100 nm layer of silver was deposited at a faster rate of 1-2 Å/s.

5.2 Device Performance

Devices have to be evaluated in aggregate because the wide variance in device quality our fabrication process procures. I believe most variation stems from our thin LiF layer. The desired 10 Å layer thickness tests the limits of our deposition monitor, which can measure no less than 0.1 Å/s, and perhaps unreliably when depositing at such low rates. Many works suggest that devices do not get full LiF coverage before 1 nm, due to the natural evaporation dynamics and chamber geometry[36]. In Figure 5.3, we see the result of increasingly thinner PEDOT:PSS layers. From red towards blue, we go from essentially zero power output to a nearly 20% power conversion efficiency. The dashed orange and blue lines show outlier behavior of 200% and 400% diluted devices. These devices seem to be in their own behavior regime, probably due to the variance of LiF deposition within the chamber. Interestingly, in the 2:1 case, efficiency improved. This was not the case for the 4:1 set of devices, perhaps due to coincidental circumstances regarding other layers (perhaps a particularly defect-free or defect-filled region of perovskite, for example).

In comparing a thinner PCBM (spun at 4000 RPM) to a thicker layer of PCBM (spun at 1500 RPM), we find an improvement in device performance from an average of 14.3% (median of 13.93%)to an average of 10.6% (median of 13.41%). This improvement in average is larger than the improvement in median values, indicating that thinner PCBM has more varied results, but with 'access' to higher possible efficiencies. This has analogs in another semiconductor industry, namely chip fabrication. The various tiers of chip quality manufactured by companies like Intel all come from the same work flow; they are just binned according to their performance once off the production line. Similarly, one might imagine choosing to optimize a hypothetical $MAPbI_3$ solar cell factory to either a) consistently produce medium tier solar cells, or to b) produce solar cells with a wider range of performance that can get binned for different markets or use cases. Research into

5.2.1 PEDOT:PSS Thickness

To get some notion of film thickness, 4-probe resistivity measurements were made. 4-probe measures the sheet resistance across a thin film. The relationship between sheet resistance R_S (extrinsic property), which is a property of a particular thin-film, and resistivity ρ_0, which is a property of the material (intrinsic

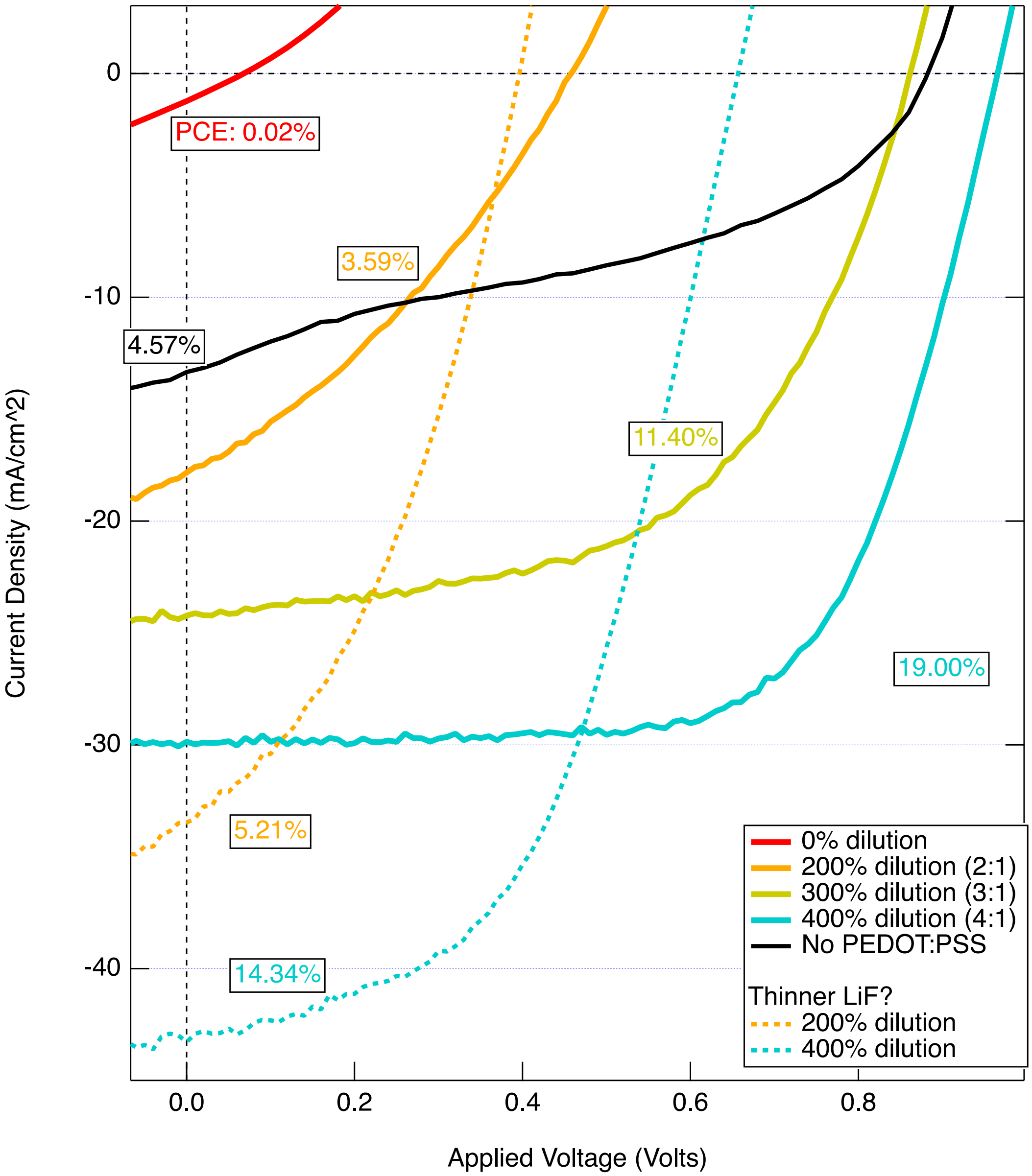

Figure 5.3: Some choice current-voltage measurements from various PEDOT:PSS dilutions. From the top-left corner towards the bottom-right, we get a progression of increasingly diluted solutions producing better devices. Note that our hero device, the solid blue line with a PCE of 19%, had a more optimized PCBM layer as well.

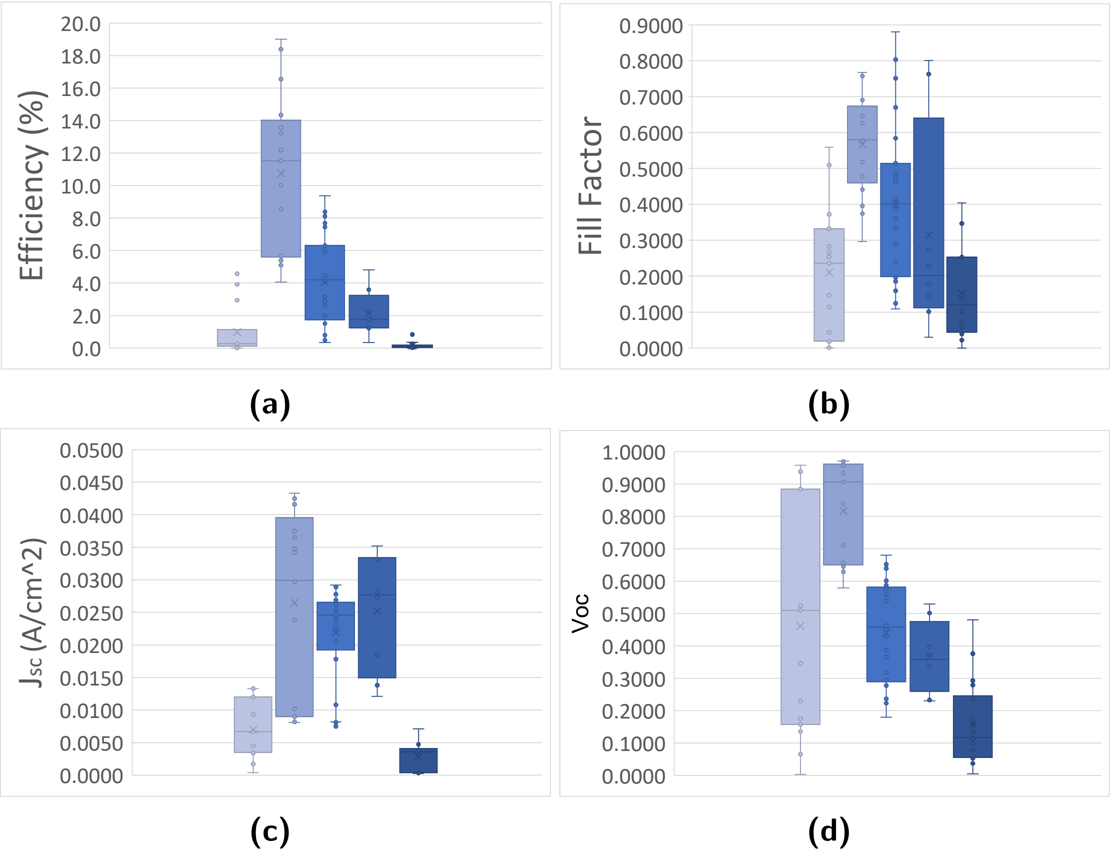

Figure 5.4: Plotted here are the (a) power conversion efficiencies, (b) fill factors, (c) the short circuit currents, and (d) the open-circuit voltages for devices fabricated with no PEDOT:PSS layer, with 400% dilution, 300% dilution, 200% dilution, and with PEDOT:PSS as is. Lightest blue corresponds to most dilution (i.e. no PEDOT:PSS) to darkest blue with no dilution.

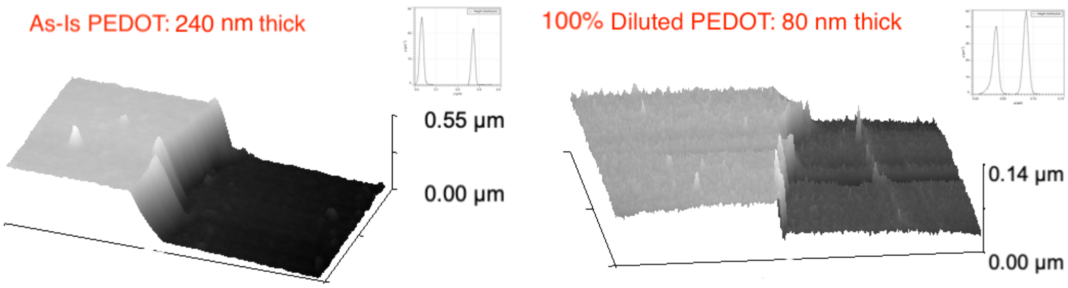

(a) As-Is **(b)** 1 H_2O: 1 PEDOT:PSS

Figure 5.5: Two PEDOT:PSS thin-films prepared on glass, a) as-shipped and b) diluted to twice the volume. Upon further dilution, AFM measurements became unreliable.

property), is shown below:

$$
\begin{aligned}
R &= \rho_0 \frac{L}{A}, \text{ where L is the length of the path traveled and A is the cross-sectional area} \\
&= \rho_0 \frac{L}{W \cdot t}, \text{ where W is the width of the cross-sectional area and t is its thickness} \\
&= \frac{\rho_0}{t} \frac{L}{W}, \\
R &= R_s \frac{L}{W}, \text{ where } R_s = \rho_0 / t \ .
\end{aligned}
$$

For a square sample where $L = W$, we then get

$$R = R_s = \rho_0 / t. \tag{5.1}$$

This can be described as a geometric representation of sheet resistance. To derive resistivity from current voltage measurements, we use Equation 5.2. When samples are much thinner than the spacing of your probes (our spacing is 62.5

mills between 4 colinear probes), the relationship between ρ_0 and your voltage measurement is

$$\rho_0 = \frac{\pi}{\ln(2)} t \frac{\Delta V}{I}, \tag{5.2}$$

where $\frac{\pi}{\ln 2}$ is a consequence of the tip and sample geometry (see `here` for more theory regarding 4-point probes). Therefore, if we know ρ_0, which again is a property of the material and should hold true for any thickness of PEDOT:PSS, we can approximate the thickness of all our PEDOT:PSS layers. To test this, I measured the thickness of our two thickest samples, the non-diluted and the 1:1 sample. The AFM measurements are shown in Figure 5.5. According to spin coater manufacturer Ossila,"At low concentrations the thickness of a film is approximately linearly dependent upon the concentration of the material in the ink, however as concentrations increase this will affect the viscosity of the ink and thus a non-linear relationship will develop"[17]. However, we do not know what that critical concentration is. Qualitatively, the as-is solution acts more like ink than thin solution, preferring to stay where dropped on a substrate rather than spread. This would indicate that the initial concentration might cause irritably thick layers. Indeed, we find a nonlinear relationship from our AFM data. As seen in Figure 5.5a, we found our PEDOT layer to be 240 nm when undiluted; the half-as-concentrated sample, in Figure 5.5b is 80 nm. This is 30% lower than the expected thickness given the original sample. Since we have measured $\Delta V/I$,

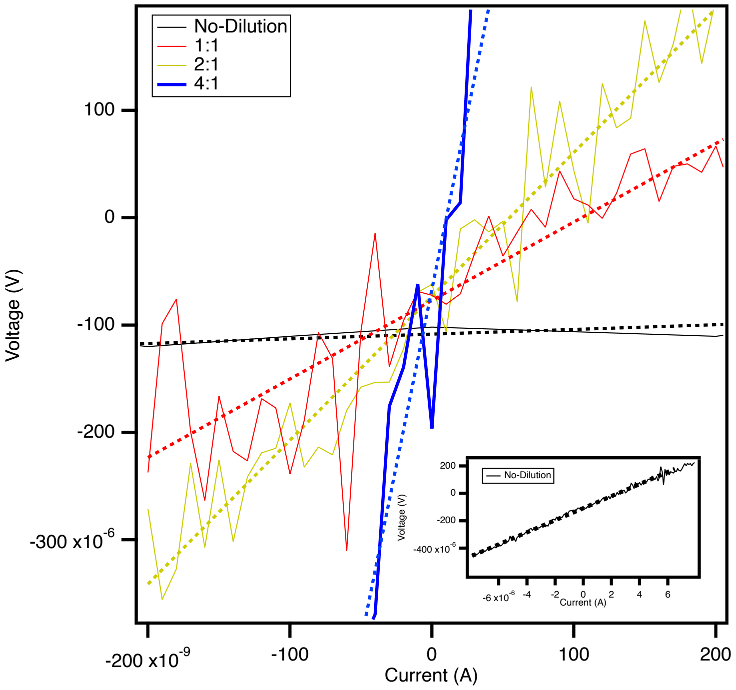

Figure 5.6: Voltage-vs-current measurements on PEDOT:PSS thin-films of various dilutions. These measurements were made *via* a 4-point probe on 1 in^2 glass susbtrates. The subwindow shows a close-up of the non-dilution trace on a different scale, as it appears flat on the voltage range needed to display the diluted films.

shown in Figure 5.6 we can use Equation 5.2 to calculate responsivities.

We may extrapolate the thicknesses in two ways: 1) we may assume the resistivity ρ_0 measured with the known thickness data is true for all films, or 2) we may assume thickness scales linearly beginning with the 1:1 solution. Neither of these lead to practical results. Indeed, for the only two samples for which we have both thickness and sheet resistance measurements, their responsivities differ greatly. Using Equation 5.2 with the resistances found in Figure 5.6, we find the non-diluted responsivity to be 0.004 $\Omega\cdot$ cm. Meanwhile, the 1:1, with its 20x higher sheet resistance but only 3x reduction in thickness, is approximately 0.03 $\Omega\cdot$ cm. Below, we have two tables showing the results of these two extrapolations. In the first, ρ_0 is assumed constant, which provides non-physical thicknesses of 0.1 nm for our thinnest sample. The second table provides more reasonable thickness estimates, given a linear relationship between thickness and concentration, but has quickly increasing ρ_0.

Assuming equal resistivities ρ_0:

Rel. conc.	thickness (nm)	R$_s$	ρ_0
1	240.0	91	21744.0
0.50 (1:1)	1.1	19977	21744.0
0.33 (2:1)	0.3	86070	21744.0
0.20 (4:1)	0.1	199320	21744.0

Table 5.1: Extrapolated thickness values keeping ρ_0 constant. We see very dubious results for relative concentrations that span only half an order of magnitude.

Assuming linear relationship between concentration and thickness:

Rel. conc.	thickness (nm)	R$_s$	ρ_0
1	240.0	91	21744.0
0.50 (1:1)	80.0	19977	1598184.0
0.33 (2:1)	52.8	86070	4544496.0
0.20 (4:1)	32.0	199320	6378240.0

Table 5.2: Extrapolated thickness from the 1:1 value, assuming a linear relationship between concentration and thickness. We see very extreme changes in resistivity for relative concentrations that span only half an order of magnitude.

Chapter 6

Organic-Inorganic Perovskites in Light-Emitting Diodes

Organic-inorganic halide perovskites have garnered much attention for their superb optoelectronics properties, including their high luminescent color purity[37], high charge mobility[38] (relative to their needed thicknesses), and large photoluminescent quantum yield[6]. They may be fabricated easily into thin-films *via* solution processing, and their bandgaps are tunable by halide composition[39]. Consequently, perovskites have great promise as emission layers in metal-insulating-metal light-emitting diodes. In this work, we understand the minimum surface quality needed to obtain working perovskite LEDs.

6.1 Introduction

The primary figure-of-merit for PeLEDs, and LEDs in general, is their external quantum efficiency, or EQE. This is defined to be

$$\mathrm{EQE} = \frac{\text{number of photons out}}{\text{number of electrons in}} = \frac{\dot{N}_\gamma}{\dot{N}_e}. \tag{6.1}$$

This is a measurement of how well injected charge carriers are undergoing radiative recombination, i.e. how well are we converting electrons and hole pairs into photons. While radiative recombination is the goal, there are nonradiative recombination mechanisms that stand in our way. Chiefly, trap-assisted recombination is a concern. These are interband (Figure 6.1) states that excited electrons or holes relax to *via* lattice vibrations. These so-called *trap states* can be purposefully added through doping, or might be unfortunate consequences of unwanted defects.

Whether its existence is intentional or not, a trap state may be generally binned as a shallow or deep trap state. As a rule of thumb, shallow trap states sit close to a band edge, on the order of $k_BT \approx 25meV$ for room temperature. Those traps that are within k_BT below the conduction band are electron traps, while those within k_BT of the valence band are hole traps. Trap states farther out from a band edge than k_BT are generally considered deep trap states. Deep trap states are generally considered more concerning, as they can act as traps to both electrons and holes and consequently are more likely to induce nonradiative recombination

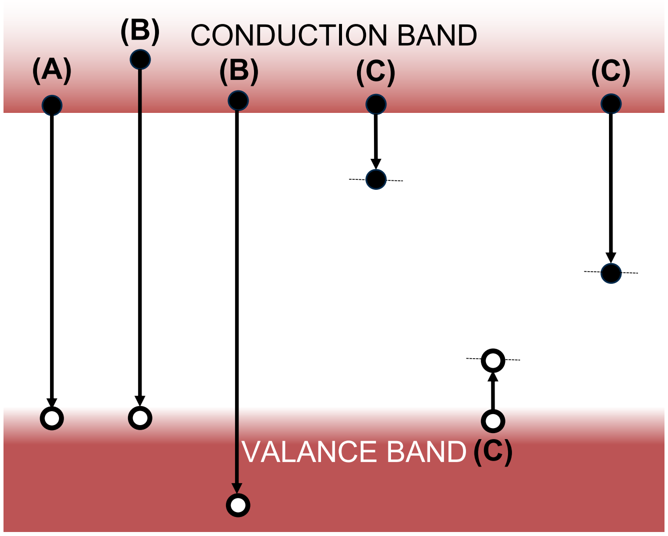

Figure 6.1: Schematics of (A) edge-to-edge recombination, (B) "hot" electron relaxation, emitting a photon $E_\gamma > E_{\mathrm{BG}}$, (C) shallow and deep trap states that prevent radiative recombination.

[40]. Myriad research suggests perovskite to be *defect tolerant* [41]. Reference [40] argues that more recent first-principal calculations suggest perovskite to be as defect *intolerant* as conventional semiconductors, but it has a remarkably low defect density despite its low temperature processing. It is perhaps most agreeable then to say that perovskites are quite robust against a quite "messy" fabrication process, and even lacking a proper clean room setting, or pure precursors, one can achieve quite good performance with low temperature processing.

6.2 Previous work on PeLEDs

Organic-inorganic perovskite was first utilized as a solar cell in 2009, and received much attention in its capacity as a PV material. It was not until 2014 when work on the first room-temperature perovskite LED (PeLED) was published[42]. This device was based on the traditional perovskite solar cell architecture, which has the active perovskite layer sandwiched between a TiO_2 electron transport layer (ETL) and an organic hole transport layer(HTL). Since then, other device architectures have been utilized, including so-called "reverse structures", i.e. p-i-n devices[43].

6.2.1 Comparing and Constrasting Solar Cell Optimization

Given that Tan. *et. al.*, and others since, use the solar cell architecture to make functional LEDs, it may seem that creating photons rather than absorbing them is as easy as flipping the voltage. It is indeed true that a charge transport layer, if it makes an ohmic contact with the active layer, should successfully carry charge in either direction. However, there are other factors that must be reconsidered.

One critical difference is recombination. A solar cell's job is to prevent recombination at all costs, whereas an LED wants to make sure that oppositely charge carriers meet and annihilate radiatively. Solar cell literature has found that excess lead in the system (*via* a precursor solution where Moles $PbI_2 >$ moles FAI), increases power conversion efficiencies. Arguments have been made that excess lead is deposited in the grain boundaries, where it helps increase carrier lifetimes, giving photogenerated charge carriers times to reach device electrodes [44]. Work by Park *et. al.*[45] finds that excess PbI_2 leads to slightly larger grain sizes, better oriented grains, and lower recombination, despite no significant difference in diffusion lengths. This aligns well with PeLED work that suggests that smaller grain sizes helps increase the EQE of PeLED devices, such as in Reference [46] where Kim *et. al.* systematically changes grain size using various intensities of laser annealing. It is not surprising then that PeLED researchers unbalance the moalr ratio in the opposite direction, adding excess organic iodide (MABr, FABr) to counteract the effects of free lead[8].

Additionally, whereas solar cells are made to be as thick as diffusion lengths allow (to maximize absorption without encouraging recombination), LEDs EQE generally benefits from being thinner, on the tens of nanometers. This way, we minimize photon absorption. However, it should be noted that too thin of an emission layer might result in pinholes and decreased recombination. These two characteristics, recombination rates and layer thickness, are examples of how optimizing solar cell and LED devices often requires opposite treatment.

6.2.2 Tunability through Composition

Many variations on the perovskite active layer have been used since 2014, mostly tuning the composition of the X-site to achieve certain wavelengths in the infrared and visible regime. All else being equal, replacement of the commonly used lead for tin increases the possible bandgap wavelengths in organic-inorganic PeLEDs from 800 to 950 nm[6]. Near-infrared emitters beyond 950 nm can be achieved only with the introduction of NIR-emitting dopants, such as ytterbium or PbS quantum dots. The wide swath of fabricated PeLEDs, with their respective peak emission wavelengths and external quantum efficiencies, is summarized in Figure 6.2.

While all LED colors may find use, whether it be in manufacturing (UV in curing, lithography, 3D printing), display technologies (visible wavelengths in TVs and smartphones), or in medical sensors (near-IR in oxygen sensors and imaging)[6], the Department of Energy has highlighted `on their website` the "Green Gap", the efficiency deficit green LEDs have relative to other visible wavelengths LEDs.

For this reason, I investigated Green LEDs emission layers. For a pure green emission in an ABX_3 perovskite material, it is appropriate to use bromine in the halogen X site. While much work was done with a methylammonium (CH_3NH_3) A site, it has been shown that formamidinium ($(NH_2)_2CH$) has been found to be

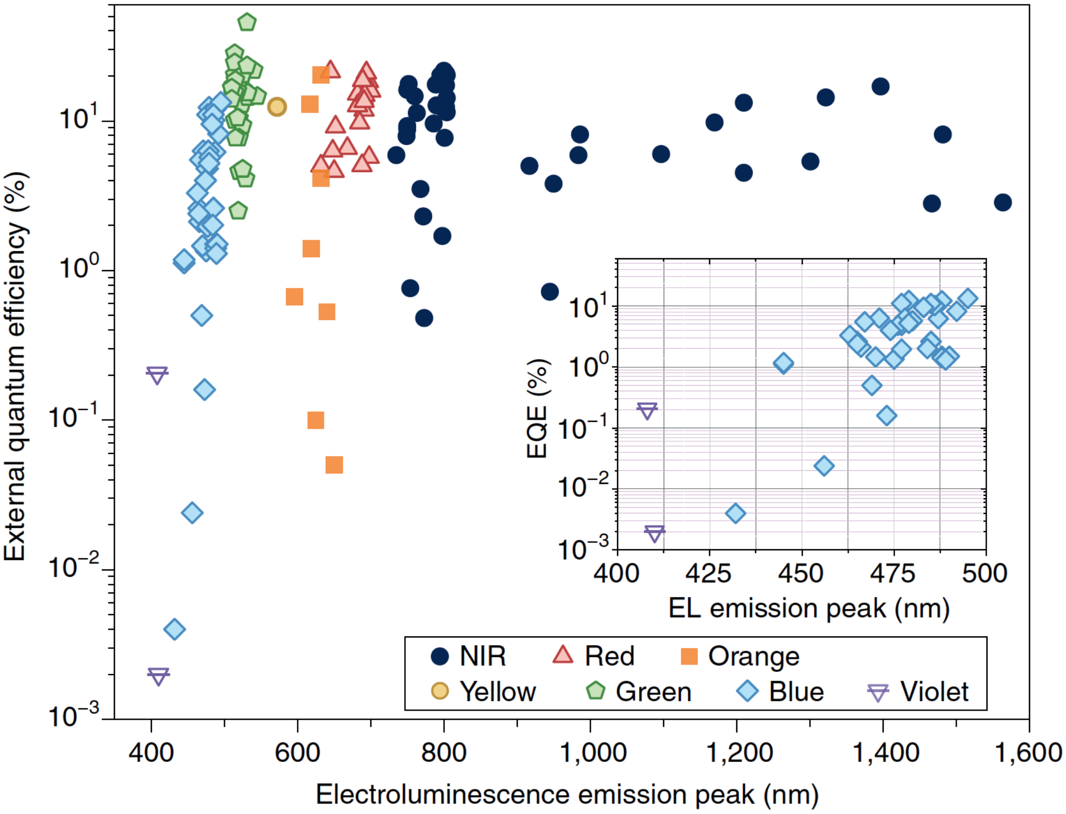

Figure 6.2: Summarizes the peak emission wavelength of various PeLEDs along with their respective quantum efficiencies. From Reference [6], with literature sources tabulated in the paper's supplementary information document.

more thermally stable [47].

6.3 Device Fabrication

6.3.1 SpiroOMeTAD Preparation:

I mix 72.3 mg Spiro-OMeTAD in 1 mL chlorobenzene. In a separate vial, I dissolve a precursor solution of 520 mg lithium bis(trifluoromethylsulfonyl)imide (LiTFSI) in 1 mL acetonitrile. Once the LiTFSI has dissolved, I add 17.5 µL of LiTFSI solution to the Spiro-OMeTAD solution. To this Spiro-OMeTAD vial, I finally add 28.8 µL of 4-tert-butylpyridine. This solution is stirred at room temperature for 1 hour.

6.3.2 Perovskite Preparation

Perovskite solutions were prepared in a stoichiometric molar ratio of 1 $PbBr_2$: 1.x FABr : 4 DMSO : 17 DMF, where 1.x is varied from 1.0 to 1.5. To begin with, FABr powder (Sigma Aldrich) is first dissolved in dimethylformamide (DMF) with a 4.0 M concentration. In another vial, dry 1 mole $PbBr_2$ is placed and measured. I then dissolve the $PbBr_2$ in 4 moles of DMSO and some amount of DMF (17 moles minus the contribution from the FABr solution to be added later). The $PbBr_2$ is stirred overnight at 70 C. After the $PbBr_2$ is dissolved, the stoichiometrically appropriate amount of 4 M FABr solution is added[1]. [1]

6.3.3 Perovskite Film Fabrication

All glass substrates, whether pristine or etched with patterned ITO, were cleaned using detergent, followed by sequential 15 minute sonication baths in acetone and isopropanol. 30 µL of perovskite solution would be dropped on our substrate, which was then spin cast at 5000 RPM in a nitrogen-filled glovebox. As shown in Figure 6.5a, which is borrowed from Reference [7], 200 µL of toluene is dropped 4 seconds after the spinning begins. The substrate is spun for 50 seconds. The films is then dried at 60 C for 10 minutes.

6.3.4 Device Fabrication

Glass slides with etched ITO were cleaned in the manner described above. TiO_2 (Solaronix) was applied using a screen printing technique. The perovskite was then spin cast in the manner described above. A Spiro-OMeTAD (Sigma Aldrich) layer is then spin cast using 30 µL of solution spun for 30 seconds at 3000

---

[1] As an example calcuation, if we wanted a solution with a molar ratio of 1 $PbBr_2$: 1.2 FABr, we begin by measuring 1 mole of $PbBr_2$ in a vial. I will then add 4 moles of DMSO (284 mL) and 13.1 moles of DMF (1.02 L), with the remaining DMF to be contributed from the FABr solution. After dissolving the $PbBr_2$, we add

$$1.2 \text{ moles FABr} \times \frac{1 \text{ liter}}{4 \text{ moles FABr}} = 300\text{mL}$$

of the FABr solution, which accounts for the remaining needed DMF.

RPM in a nitrogen-filled glovebox. Devices were then brought out of the glovebox and stored in an air-filled dry box for 24 hours, so that the Spiro-OMeTAD layer may be oxidized, as recommended for hole transport improvements[48]. The devices are then returned to the glovebox where a 100 nm Au layer is thermally evaporated on our devices. Devices are then tested in the glovebox.

6.4 Work and Results

6.4.1 Device Architecture

We implemented this perovskite layer into two device architectures: initially we tried the 'reverse' p-i-n architecture (Figure 6.3a), where the light-facing glass sits under a p-type conductor, namely PEDOT:PSS, the intrinsic absorption layer $FAPbBr_3$, and the electron-favoring calcium. This p-i-n architecture is common to the OLED research sector [49, 50].

Also used is the n-i-p (Figure 6.3b, as seen in Reference [51], wit TiO_2 and Spiro-OMeTAD respectively guiding electrons and holes towards the absorption layer. This n-i-p type is typical for perovskite solar cell and dye-sensitized solar cell research; thanks to its favorable conduction edge and deep valence edge, TiO_2 is concurrently an n-type injection layer and a p-type blocking layer. This is complimented by a semiconducting polymer, namely Spiro-OMeTAD, which is a good hole conductor but poor electron conductor.

As the goal is efficient charge injection, we must have charge injection layers that have energy levels favorable to $FAPbBr_3$. As can be seen in Figure 6.3a, there are a few problems with the p-i-n type; the holes are ejected from the ITO towards the valence band, they have to jump not one but two higher energy states to reach the $FAPbBr_3$ valence band. Meanwhile the electrons should have no trouble being injected from the calcium to the perovskite's conduction band. Besides this energy-level mismatch, another issue arises: we find that all our assistant layers (electrodes, injection layer) are conducting. Indeed, it might be that the layers here are *too* conductive. Indeed, work by Wang *et. al.* [8] showed that using a more resistive PEDOT:PSS leads to a better performing device. Additionally, there are no semiconducting blocking layers preventing hot charge carriers from avoiding recombination and passing through the device unabated.

This could explain the lack of radiative recombination I experienced with our p-i-n device type, as I was not able to achieve electroluminescence. This is evidenced by the higher currents seen in the p-i-n devices as compared to the n-i-p devices (Figure 6.4) in the sub-bandgap voltage regime. With this information in hand, I ultimately pivoted to exclusively using the n-i-p architecture.

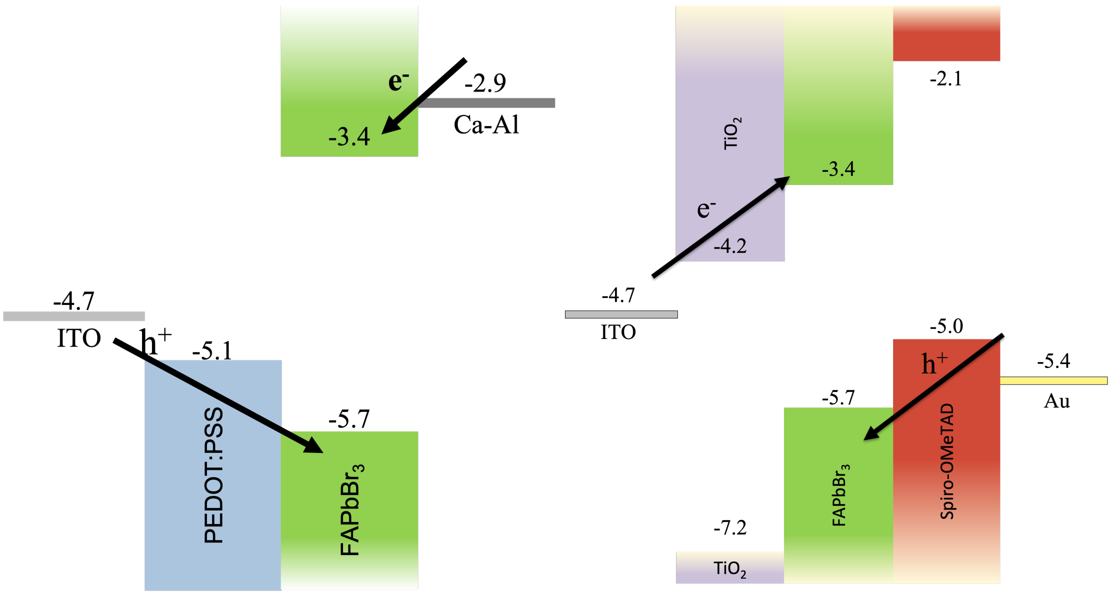

(a) p-i-n architecture

(b) n-i-p architecture

Figure 6.3: The energy levels associated with the two device architectures explored, with a) often referred to as as reverse architecture, and b) the more conventional architecture.

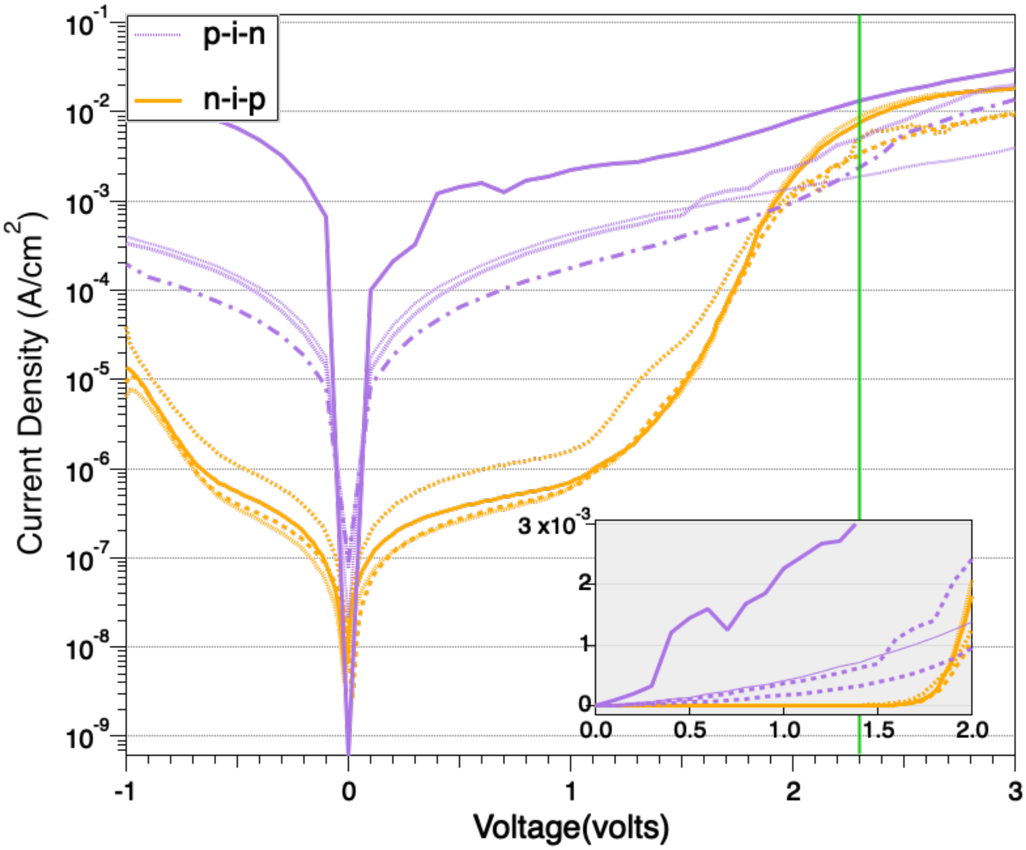

Figure 6.4: A semi-log J-V plot showcasing an ensemble of devices using the p-i-n (purple) and n-i-p (yellow) architectures. We see that, for low currents, the p-i-n architecture magnitudes more of current. The lack of proper blocking layers in the p-i-n architecture might lead to current passing through the device without recombination. The subfigure showcases the same plot on linear axes. The green line highlights the bandgap voltage 2.3 V for $FAPbBr_3$.

6.4.2 Exploring Perovskite Preparation and Stoichiometry

Initial work naively used a stoichiometric ratio of perovskite precursors outlined by Das *et. al.*[51] in 2017. Their work concerned fabricating solar cells, and was thus optimized for a thick absorption layer and excess $PbBr_2$. Understanding the benefits of a non-stoichiometric ratio of precursor when I came across the work of Wang *et. al.*[8], whose work uses a one-step solvent engineered fabrication process (as described in Section 6.3.3), with precursors dissolved in a 1 $PbBr_2$: 2 FABr molar ratio. This excess FABr helps guarantee that no free lead is present in the system. We want to encourage recombination, and if excess Pb prevents that, we are to make sure it is not there.

We compare our replication by checking that we are in fact making $FAPbBr_3$. As seen in Figure 6.5b, UV exposure indeed causes a green luminescence. This is confirmed through absorption and photoluminescence spectroscopy; my $FAPbBr_3$ measurements are compared with Wang *et. al.* in Figures 6.6a and 6.6b. We can see in Figure 6.6b that our luminescence peak lines up well with the absorption edge, suggesting the film is absorbing photon energies equal to or great than the bandgap energy, and re-emitting these photons at the bandgap energy. We use the peak emission in Equation 6.2 to estimate our optical bandgap as

$$E_{\mathrm{BG}} = \frac{hc}{\lambda} = \frac{1240\ \mathrm{eV} \cdot \mathrm{nm}}{540\ \mathrm{nm}} = 2.3\ \mathrm{eV}. \tag{6.2}$$

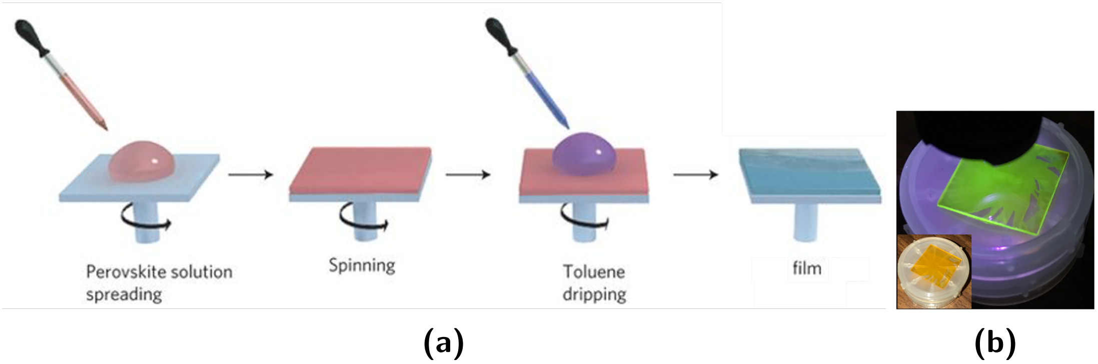

Figure 6.5: a) Schematic of the one-step solvent engineer process spearheaded by Jeon *et. al.* [7]; this diagram is borrowed from their work. b) $FAPbBr_3$ film spun on glass, with and without UV light.

Our final analysis of the thin-film on glass is not an optical measurement, but a surface measurement *via* atomic force microscopy. I was very surprised to find that the surface roughness was an astounding 40 nm, especially concerning since we strive to have our LED emission layers as thin 80 nm!

However, it explains why we were not able to get light emission while other researchers did, even when using a large amount of excess FABr. Wang *et. al.*'s emission layer, for example, is just shy of 300 nm. While this makes for robust coverage, and prevents pinholes even with such a rough surface, it leads to inefficient emission[52]. If we want efficient devices, we must not compensate for the large roughness with a thick sample; we must fix the roughness. A smoother surface would also have a secondary positive effect, decreasing trap states at the perovskite/Spiro-OMeTAD interface that interfere with charge injection.

Interpolating between the stoichiometric sample and the +100% excess FABr

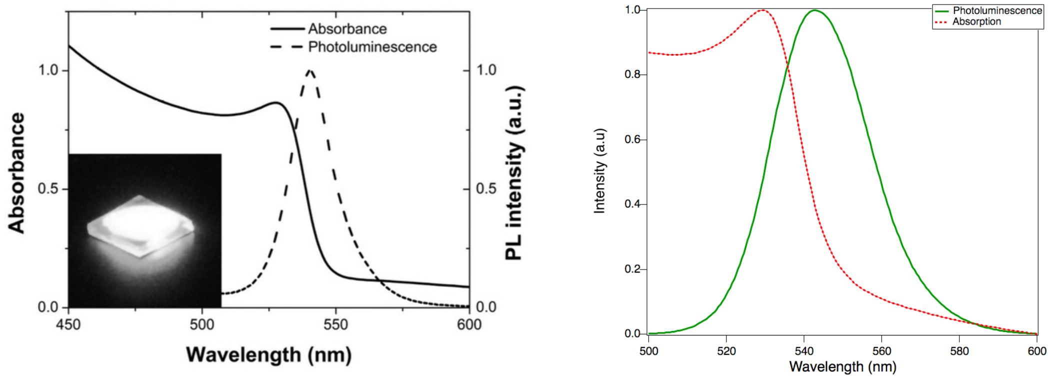

(a) (b)

Figure 6.6: a) the photoluminescence and absorption spectrum of FAPbBr$_3$ found by Wang *et. al.*[8]. b) My own spectroscopy measurements, finding an identical spectrum.

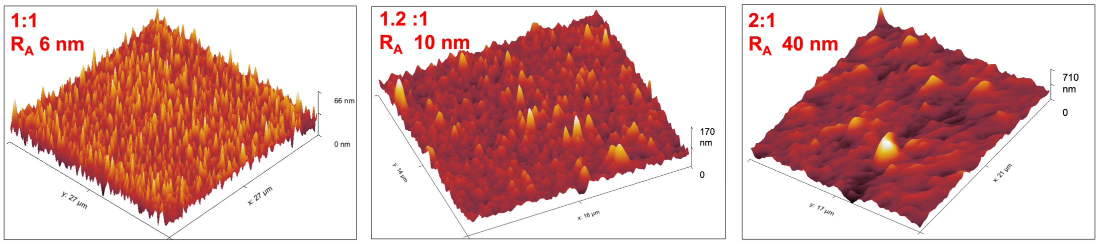

(a) (b) (c)

Figure 6.7: Roughness measurements for FAPbBr$_3$ composed with a) 0% excess FABr, b) 20% excess FABr, and c) 100% excess FABr. Note that each Figure is scaled to its own range of values, so the stoichiometric sample's spikey appearance is in fact smooth.

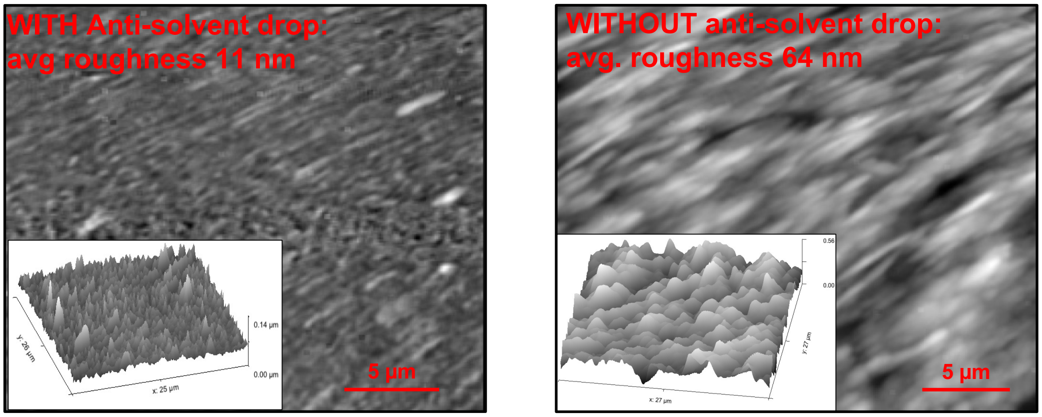

(a) **(b)**

Figure 6.8: FAPbBr$_3$ thin films with and without an anti-solvent drop 4s after beginning to spin the substrate. We see a 5x decrease in surface roughness when an anti-solvent is used. A smooth surface is an important condition for charge injection and radiative recombination.

sample (Figure 6.7c), I prepared samples with only 20% excess FABr 6.7). We find they suffer very little for the excess FABr, with a surface roughness of only 10 nm.

6.4.3 Optimizing Anti-Solvent Drop Time

In the first few seconds of the spin process, an antisolvent is dropped, which accelerates solvent evaporation. The difference in film morphology can be seen in Figure 6.8, where our 1-step sample with an antisolvent drop had an average roughness of 11 nm, in contrast with the '1-step-only' sample with a roughness of 64 nm.

One parameter that seems to vary from lab to lab is the time you wait to drop the anti-solvent onto the already-spinning substrate. I optimize this parameter by seeing how photoluminescence is affected if anti-solvent is dropped at 3s, 4s, and 5s (Figure 6.9) The small window of acceptable drop time is certainly a drawback to the 1-step process. Research by Taylor *et. al.*[53] suggests that one critical parameter for toluene drop time is the duration of the drop, even if using the same volume of anti-solvent. They argue in their 2021 work that, due to toluene's low miscibility with DMF, expelling the toluene from the pipette too quickly doesn't allow the toluene to encourage DMF evaporation. Despite this narrow window, and our manual pipette dispensing, I am able to show that dropping toluene after 4s is almost always the best for our $FAPbBr_3$ samples.

6.4.4 Trap States as a Function of Stoichiometry

Note, this data was collected by Dr. Kaitlin Hellier for samples prepared by me.

Using a photothermal deflection spectrometer, one can use its much more sensitive probing to better estimate band gaps and lattice disorder for our samples. In Figure 6.10, PDS data was collected for samples with 0% to 50% excess FABr. The largest urbach energy is found in perovskite samples prepared with an even ratio of precursors, suggesting that unreacted $PbBr_2$ is causing general disorder in our system. Disorder is greatly suppressed as soon as we add just 10-20%

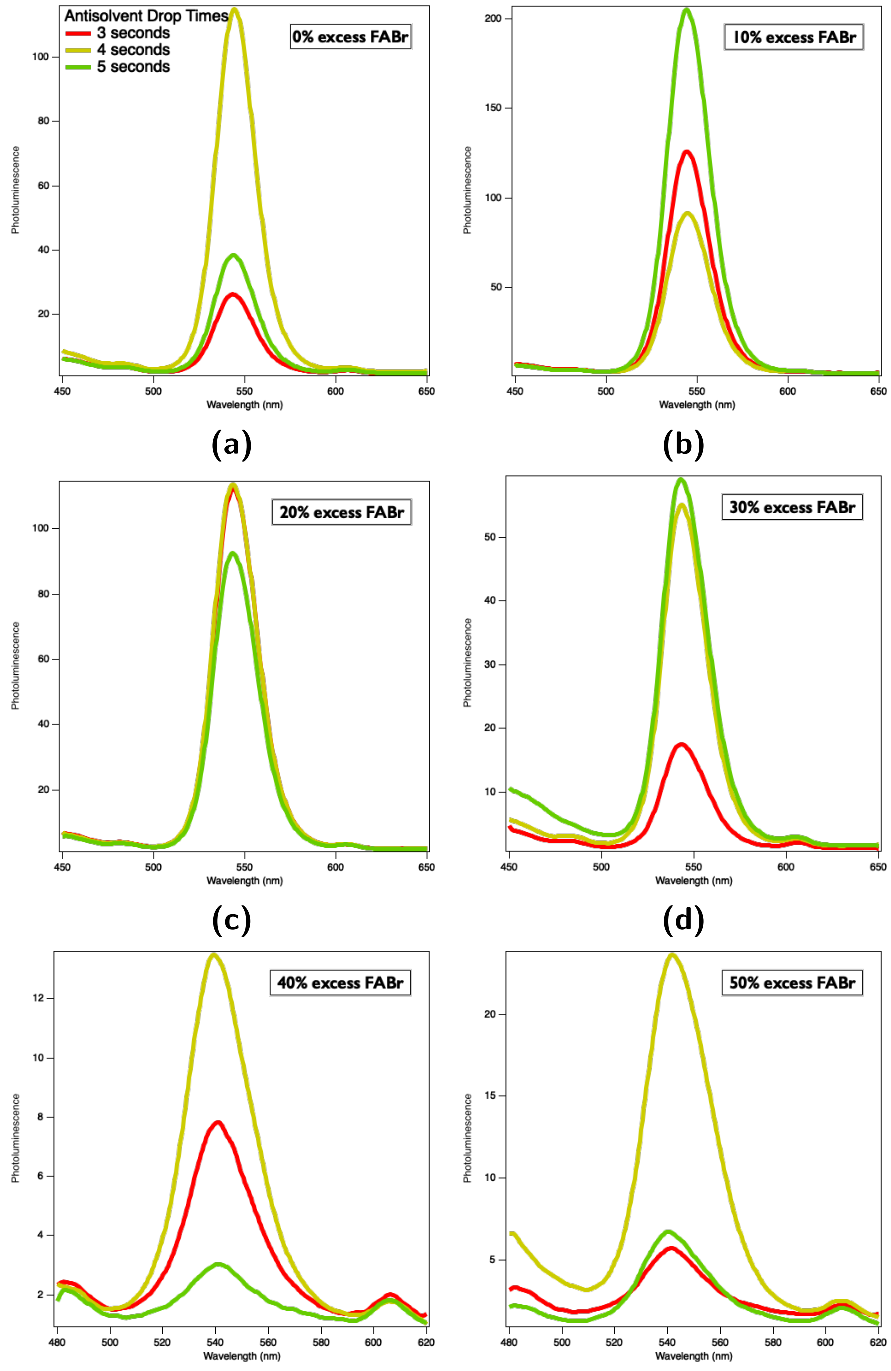

(a) (b)

(c) (d)

(e) (f)

Figure 6.9: Toluene anti-solvent drop times at t = 3s (red), 4s (yellow), and 5s (green) for samples with 0% to 50% excess FABr. We see that for nearly all samples, a 4s drop time is the most effective for maximizing photoluminescence.

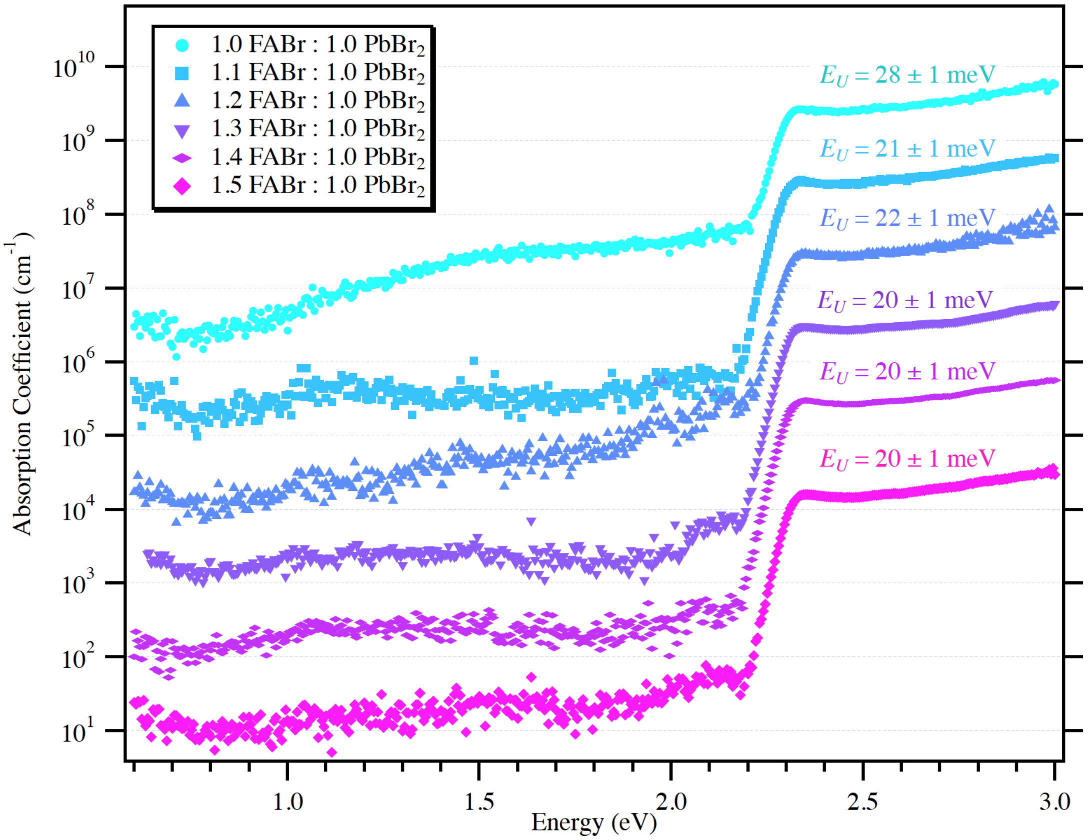

Figure 6.10: Photothermal deflection spectroscopy results for FAPbBr$_3$ films prepared with 0-50% excess FABr precursor. Fitted with a direct tauc plot, all samples measured an optical bandgap of 2.8 eV.

excess FABr, lowering the urbach energies by about 25%. Beginning at 30% excess FABr, urbach energies stabilize at 20 meV. Since PDS is a bulk measurement, this confirms that our luminescence issues are likely due to surface morphology. Likely, a combination of pinholes and interface states induced by the rough FAPbBr$_3$ surface is leading to radiation suppression.

6.4.5 Device Performance

Finally, we can put all this work together and get performing devices. Once the surface roughness was reduced, while keeping our device thin and free of unreacted Pb, devices were repeatedly acheivable. This process was robust, with 23 out of 24 devices providing light.

A schematic suggesting how light intensity was measured is shown in Figure 6.11a. Figure 6.11b plots the current-voltage measurement of a working device, and the photocurrent it drives in a photodetector sitting above the PeLED. The immediate standout behavior is that the photocurrent remains low, until a critical voltage around 1.7V that is coincident with the increase in current seen in the PeLED. This indicates that photons are being created substantially before the emission layer's bandgap energy. This has been observed in other works[8, 54] and is ascribed to an auger-assisted injection process.

This succesful PeLED is summarized in its electroluminescence spectra seen in Figure 6.11c. We see a narrow Full-Width-Half-Maximum of 24 nm, in line with industry standards. This high color purity is showcased in the CIE plot in Figure 6.11d. In a CIE plot, a spectra is summarized as a single point in this color space. The perimeter of this colorful manifold represents monochromatic light; the center represents the addition of all wavelengths of light. We see that our spectra neighbors the 540 nm pure light region of the CIE space.

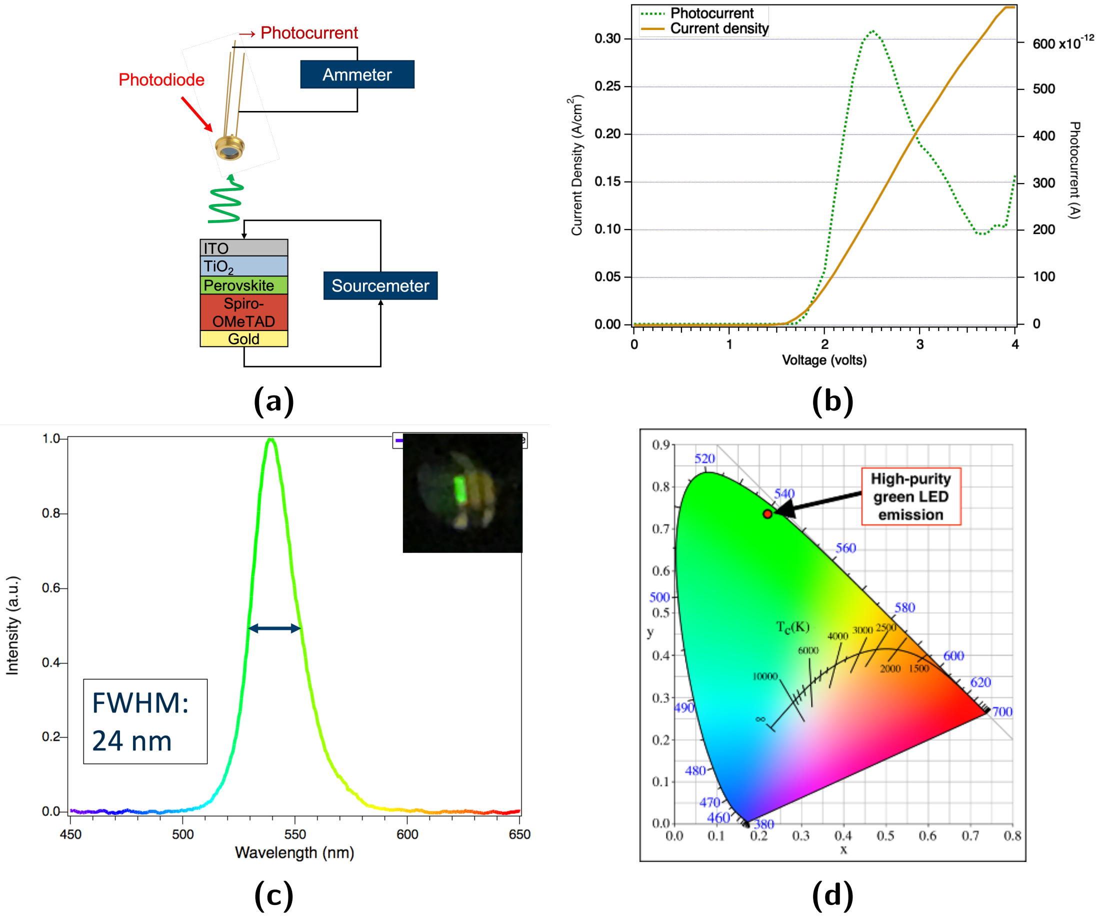

(a) (b) (c) (d)

Figure 6.11: a) A schematic showing that the photocurrent is producing light which is being measured by a photodiode; b) The photocurrent produced by the photodetector (green), measuring the quantity of light being produced by the working PeLED's injected current (brown); c) Electroluminescence spectra with a Full-Width-Half-Maximum of 24 nm, and inset photograph of an operating PeLED; d) CIE plot showing high color purity of 540 nm.

Chapter 7

Conclusion

In these works, we explored the fabrication methods and performances of various thin-film optoelectronics. We modeled germanium quantum dots to understand their size dispersions. We also explored how a quantum dot's size and crystallinity affects bandgap and disorder energies. It was found that the increased crystallinity associated with our collaborators' new synthesis method allowed for increased currents for a given bias, resulting in a higher signal-to-noise.

Quantum dots have a future in technology. Even now, they are used as passive emitters in LCD TVs (marketed as QLED). With bandgaps tunable by size (and size tunable by varying temperature, dopant levels, or ligand precursors), we we can see why there is such interest in using them in optoelectronics. A hypothetical manufacturer could change simple parameters in their process to get desired optical properties. One could imagine custom order LEDs an detectors!

Perovskite optoelectronics were also investigated in these works. Organic-inorganic halide perovskites have many attractive features as solar cell absorption layers. Amongst others properties, their high absorption, low temperature fabrication, long possible diffusion lengths, and ultimately low-cost make them very attractive for next-generation solar cells. We explored how to best leverage the hole transport layer, investigating the benefits gained from making it continuously thinner. With devices 500 nm thick, we can truly say these are thin-film devices, being 400-1000 times thinner than traditional silicon solar cells!

While our PV work considered how to best get electrons out of photons, our LED work studied turning electrons into photons. Interested in green photons, this work explored the use of $FAPbBr_3$ as the emission layer in thin-film light-emitting diodes. We found that the quality of the interface is extremely important, with surface roughness impacting whether not photons were emitted.

This work highlights the best that perovskites has to offer. This research was very “dirty”, and did not take place with much control. There were no bunny suits involved, solvents and and solutes were often old, etc. Whether it is because of a natural disinclination towards traps, or because they are truly defect tolerant, perovskites are robust to less pure and less clean precursors and environments. This is good, and if they were ever to come to market, perovskite solar cells price point will hopefully reflect these benefits.

Our findings reinforced how solution processing, a much cheaper fabrication route than what it takes to make inorganic optoelectronics, is a worthwhile pathway towards PV fabrication. Such simple toggles, like transport layer concentration or precursor ratios, leads to great improvements in device performances.

Bibliography

[1] Simon M Sze, Yiming Li, and Kwok K Ng. *Physics of semiconductor devices.* John wiley & sons, 2021.

[2] Doris Segets, J. Matthew Lucas, Robin N. Klupp Taylor, Marcus Scheele, Haimei Zheng, A. Paul Alivisatos, and Wolfgang Peukert. Determination of the quantum dot band gap dependence on particle size from optical absorbance and transmission electron microscopy measurements. 6(10):9021–9032.

[3] V. A. Volodin, D. V. Marin, V. A. Sachkov, E. B. Gorokhov, H. Rinnert, and M. Vergnat. Applying an improved phonon confinement model to the analysis of Raman spectra of germanium nanocrystals. *Journal of Experimental and Theoretical Physics*, 118(1):65–71, January 2014.

[4] Katayoon Tabatabaei, Alexandra L. Holmes, Kathryn A. Newton, Elayaraja Muthuswamy, Roy Sfadia, Sue A. Carter, and Susan M. Kauzlarich. Halogen-

induced crystallinity and size tuning of microwave synthesized germanium nanocrystals. 31(18):7510–7521.

[5] Zheng Ju, Xiao Qi, Roy Sfadia, Minyuan Wang, Emily Tseng, Elizabeth C. Panchul, Sue A. Carter, and Susan M. Kauzlarich. Single-crystalline germanium nanocrystals via a two-step microwave-assisted colloidal synthesis from GeI4. Publisher: American Chemical Society.

[6] Azhar Fakharuddin, Mahesh K. Gangishetty, Mojtaba Abdi-Jalebi, Sang-Hyun Chin, Abd. Rashid bin Mohd Yusoff, Daniel N. Congreve, Wolfgang Tress, Felix Deschler, Maria Vasilopoulou, and Henk J. Bolink. Perovskite light-emitting diodes. *Nature Electronics*, 5(4):203–216, April 2022.

[7] Nam Joong Jeon, Jun Hong Noh, Young Chan Kim, Woon Seok Yang, Seungchan Ryu, and Sang Il Seok. Solvent engineering for high-performance inorganic–organic hybrid perovskite solar cells. *Nature Materials*, 13(9):897–903, September 2014.

[8] Juanhong Wang, Chen Song, Zhiwei He, Chaohuang Mai, Gancheng Xie, Lan Mu, Yangke Cun, Jiali Li, Jian Wang, Junbiao Peng, and Yong Cao. All-solution-processed pure formamidinium-based perovskite light-emitting diodes. *Advanced Materials*, 30(39):1804137, 2018.

[9] Steven H. Simon. *The Oxford Solid State Basics.* Oxford University Press, 2013.

[10] N. W. Ashcroft and N. D. Mermin. *Solid State Physics.* Holt-Saunders, 1976.

[11] Randy Harris. *MODERN PHYSICS.* Pearson, 2 edition, 2005.

[12] Iwan Moreels, Karel Lambert, Dries Smeets, David De Muynck, Tom Nollet, José C. Martins, Frank Vanhaecke, André Vantomme, Christophe Delerue, Guy Allan, and Zeger Hens. Size-dependent optical properties of colloidal PbS quantum dots. 3(10):3023–3030.

[13] Masaru Kuno, Irina Gushchina, Stefano Toso, and Vadim Trepalin. No one size fits all: Semiconductor nanocrystal sizing curves. *The Journal of Physical Chemistry C*, 126(29):11867–11874, 07 2022.

[14] Justinas Butkus, Parth Vashishtha, Kai Chen, Joseph K. Gallaher, Shyamal K. K. Prasad, Dani Z. Metin, Geoffry Laufersky, Nicola Gaston, Jonathan E. Halpert, and Justin M. Hodgkiss. The evolution of quantum confinement in cspbbr3 perovskite nanocrystals. *Chemistry of Materials*, 29(8):3644–3652, 04 2017.

[15] *Metal-Semiconductor Contacts*, pages 134–196. John Wiley and Sons, Ltd, 2006.

[16] N. F. Mott. Note on the contact between a metal and an insulator or semiconductor. *Mathematical Proceedings of the Cambridge Philosophical Society*, 34(4):568–572, 1938.

[17] Spin coating: Complete guide to theory and techniques. `https://www.ossila.com/en-us/pages/spin-coating`. Accessed: 2022-11-21.

[18] H. Richter, Z.P. Wang, and L. Ley. The one phonon raman spectrum in microcrystalline silicon. *Solid State Communications*, 39(5):625–629, 1981.

[19] K. Roodenko, I. A. Goldthorpe, P. C. McIntyre, and Y. J. Chabal. Modified phonon confinement model for raman spectroscopy of nanostructured materials. *Phys. Rev. B*, 82:115210, Sep 2010.

[20] Colin M. Hessel, Junwei Wei, Dariya Reid, Hiromasa Fujii, Michael C. Downer, and Brian A. Korgel. Raman spectroscopy of oxide-embedded and ligand-stabilized silicon nanocrystals. *The Journal of Physical Chemistry Letters*, 3(9):1089–1093, 05 2012.

[21] V. Paillard, P. Puech, M. A. Laguna, R. Carles, B. Kohn, and F. Huisken. Improved one-phonon confinement model for an accurate size determination of silicon nanocrystals. 86(4):1921–1924.

[22] I. H. Campbell and P. M. Fauchet. The effects of microcrystal size and shape

on the one phonon Raman spectra of crystalline semiconductors. *Solid State Communications*, 58(10):739–741, June 1986.

[23] K. W. Adu, H. R. Gutiérrez, U. J. Kim, G. U. Sumanasekera, and P. C. Eklund. Confined phonons in si nanowires. *Nano Letters*, 5(3):409–414, 03 2005.

[24] A. Wellner, V. Paillard, C. Bonafos, H. Coffin, A. Claverie, B. Schmidt, and K. H. Heinig. Stress measurements of germanium nanocrystals embedded in silicon oxide. *Journal of Applied Physics*, 94(9):5639–5642, 2003.

[25] Dmitri V. Talapin, Jong-Soo Lee, Maksym V. Kovalenko, and Elena V. Shevchenko. Prospects of colloidal nanocrystals for electronic and optoelectronic applications. 110(1):389–458. Publisher: American Chemical Society.

[26] Katayoon Tabatabaei, Heather R. Sully, Zheng Ju, Kaitlin Hellier, Haipeng Lu, Christopher J. Perez, Kathryn A. Newton, Richard L. Brutchey, Frank Bridges, Sue A. Carter, and Susan M. Kauzlarich. Structural insights on microwave-synthesized antimony-doped germanium nanocrystals. 15(1):1685–1700.

[27] Elayaraja Muthuswamy, Andrew S. Iskandar, Marlene M. Amador, and Susan M. Kauzlarich. Facile synthesis of germanium nanoparticles with size

control: Microwave versus conventional heating. 25(8):1416–1422. Publisher: American Chemical Society.

[28] Carena P. Church, Elayaraja Muthuswamy, Guangmei Zhai, Susan M. Kauzlarich, and Sue A. Carter. Quantum dot ge/TiO $_2$ heterojunction photoconductor fabrication and performance. 103(22):223506.

[29] Yiguo Yao, Caidong Cheng, Chenyang Zhang, Hanlin Hu, Kai Wang, and Stefaan De Wolf. Organic hole-transport layers for efficient, stable, and scalable inverted perovskite solar cells. *Advanced Materials*, 34(44):2203794, 2022.

[30] Thomas Webb, Stephen J. Sweeney, and Wei Zhang. Device architecture engineering: Progress toward next generation perovskite solar cells. *Advanced Functional Materials*, 31(35):2103121, 2021.

[31] Tian Du, Jinhyun Kim, Jonathan Ngiam, Shengda Xu, Piers R. F. Barnes, James R. Durrant, and Martyn A. McLachlan. Elucidating the origins of subgap tail states and open-circuit voltage in methylammonium lead triiodide perovskite solar cells. 28(32):1801808.

[32] Tian Du, Claire H. Burgess, Chieh-Ting Lin, Flurin Eisner, Jinhyun Kim, Shengda Xu, Hongkyu Kang, James R. Durrant, and Martyn A. McLachlan. Probing and controlling intragrain crystallinity for improved low temperature-processed perovskite solar cells. 28(51):1803943.

[33] Tian Du, Sinclair R. Ratnasingham, Felix U. Kosasih, Thomas J. Macdonald, Lokeshwari Mohan, Adriana Augurio, Huda Ahli, Chieh-Ting Lin, Shengda Xu, Weidong Xu, Russell Binions, Caterina Ducati, James R. Durrant, Joe Briscoe, and Martyn A. McLachlan. Aerosol assisted solvent treatment: A universal method for performance and stability enhancements in perovskite solar cells. 11(33):2101420.

[34] Zhengyi Sun, Shengwei Shi, Qinye Bao, Xianjie Liu, and Mats Fahlman. Role of thick-lithium fluoride layer in energy level alignment at organic/metal interface: Unifying effect on high metallic work functions. *Advanced Materials Interfaces*, 2(4):1400527, 2015.

[35] Zhao J. M. Zhou Y. C. Wang X. Z. Zhang S. T. Zhan Y. Q. Xu Z. Ding H. J. Zhong G. Y. Shi H. Z. Xiong Z. H. Liu Y. Wang Z. J. Obbard E. G. Ding X. M. Huang W. Hou X. Y. Wang, X. J. Enhancement of electron injection in organic light-emitting devices using an ag/lif cathode. *Journal of Applied Physics*, 95(7):3828–3830, 2004.

[36] Ayse Turak. On the role of LiF in organic optoelectronics. *Electronic Materials*, 2(2):198–221, 2021.

[37] Giulia Pacchioni. Highly efficient perovskite LEDs. *Nature Reviews Materials*, 6(2):108–108, February 2021.

[38] Carlo Motta, Fedwa El-Mellouhi, and Stefano Sanvito. Charge carrier mobility in hybrid halide perovskites. *Scientific Reports*, 5(1):12746, August 2015.

[39] Wenlei Yu, Yunfeng Jiang, Xiuwei Zhu, Chunhua Luo, Kai Jiang, Liangliang Chen, and Juan Zhang. Diversity of band gap and photoluminescence properties of lead halide perovskite: A halogen-dependent spectroscopic study. *Chemical Physics Letters*, 699:93–98, 2018.

[40] Xie Zhang, Mark E. Turiansky, Jimmy-Xuan Shen, and Chris G. Van de Walle. Defect tolerance in halide perovskites: A first-principles perspective. *Journal of Applied Physics*, 131(9):090901, 2022.

[41] Jun Kang and Lin-Wang Wang. High defect tolerance in lead halide perovskite cspbbr3. *The Journal of Physical Chemistry Letters*, 8(2):489–493, 2017. PMID: 28071911.

[42] Zhi-Kuang Tan, Reza Saberi Moghaddam, May Ling Lai, Pablo Docampo, Ruben Higler, Felix Deschler, Michael Price, Aditya Sadhanala, Luis M. Pazos, Dan Credgington, Fabian Hanusch, Thomas Bein, Henry J. Snaith, and Richard H. Friend. Bright light-emitting diodes based on organometal halide perovskite. *Nature Nanotechnology*, 9(9):687–692, September 2014.

[43] Hongting Chen, Lianwei Fan, Rui Zhang, Chunxiong Bao, Haifeng Zhao,

Wei Xiang, Wei Liu, Guangda Niu, Runda Guo, Louwen Zhang, and Lei Wang. High-efficiency formamidinium lead bromide perovskite nanocrystal-based light-emitting diodes fabricated via a surface defect self-passivation strategy. *Advanced Optical Materials*, 8(6):1901390, 2020.

[44] T. Jesper Jacobsson, Juan-Pablo Correa-Baena, Elham Halvani Anaraki, Bertrand Philippe, Samuel D. Stranks, Marine E. F. Bouduban, Wolfgang Tress, Kurt Schenk, Joël Teuscher, Jacques-E. Moser, Håkan Rensmo, and Anders Hagfeldt. Unreacted pbi2 as a double-edged sword for enhancing the performance of perovskite solar cells. *Journal of the American Chemical Society*, 138(32):10331–10343, 2016. PMID: 27437906.

[45] Byung-wook Park, Nir Kedem, Michael Kulbak, Do Yoon Lee, Woon Seok Yang, Nam Joong Jeon, Jangwon Seo, Geonhwa Kim, Ki Jeong Kim, Tae Joo Shin, Gary Hodes, David Cahen, and Sang Il Seok. Understanding how excess lead iodide precursor improves halide perovskite solar cell performance. *Nature Communications*, 9(1):3301, August 2018. Number: 1 Publisher: Nature Publishing Group.

[46] Sung Jin Kim, Jinwoo Byun, Taewoo Jeon, Hyeong Min Jin, Hye Rim Hong, and Sang Ouk Kim. Perovskite light-emitting diodes via laser crystallization: Systematic investigation on grain size effects for device performance. *ACS Applied Materials & Interfaces*, 10(3):2490–2495, 2018. PMID: 29285922.

[47] Qifeng Han, Sang-Hoon Bae, Pengyu Sun, Yao-Tsung Hsieh, Yang (Michael) Yang, You Seung Rim, Hongxiang Zhao, Qi Chen, Wangzhou Shi, Gang Li, and Yang Yang. Single crystal formamidinium lead iodide (fapbi3): Insight into the structural, optical, and electrical properties. *Advanced Materials*, 28(11):2253–2258, 2016.

[48] Ute B. Cappel, Torben Daeneke, and Udo Bach. Oxygen-induced doping of spiro-meotad in solid-state dye-sensitized solar cells and its impact on device performance. *Nano Letters*, 12(9):4925–4931, 2012. PMID: 22913390.

[49] Jorge Morgado, Franco Cacialli, Rifat Iqbal, Stephen C. Moratti, Andrew B. Holmes, Gokhan Yahioglu, Lionel R. Milgrom, and Richard H. Friend. Förster energy transfer and control of the luminescence in blends of an orange-emitting poly(p-phenylenevinylene) and a red-emitting tetraphenylporphyrin. *J. Mater. Chem.*, 11:278–283, 2001.

[50] J. M. Leger, S. A. Carter, B. Ruhstaller, H.-G. Nothofer, U. Scherf, H. Tillman, and H.-H. Hörhold. Thickness-dependent changes in the optical properties of ppv- and pf-based polymer light emitting diodes. *Phys. Rev. B*, 68:054209, Aug 2003.

[51] Jaykrushna Das, Anand S. Subbiah, Neha Mahuli, Roja Singh, and Shaibal K. Sarkar. One-step solution-processed formamidinium lead tribro-

mide formation for better reproducible planar perovskite solar cells. *Energy Technology*, 5(10):1807–1813, 2017.

[52] Monika Rai, Lydia Helena Wong, and Lioz Etgar. Effect of perovskite thickness on electroluminescence and solar cell conversion efficiency. *The Journal of Physical Chemistry Letters*, 11(19):8189–8194, 2020. PMID: 32893636.

[53] Alexander D. Taylor, Qing Sun, Katelyn P. Goetz, Qingzhi An, Tim Schramm, Yvonne Hofstetter, Maximillian Litterst, Fabian Paulus, and Yana Vaynzof. A general approach to high-efficiency perovskite solar cells by any antisolvent. *Nature Communications*, 12(1):1878, March 2021. Number: 1 Publisher: Nature Publishing Group.

[54] Lei Meng, En-Ping Yao, Ziruo Hong, Huajun Chen, Pengyu Sun, Zhanlue Yang, Gang Li, and Yang Yang. Pure formamidinium-based perovskite light-emitting diodes with high efficiency and low driving voltage. *Advanced Materials*, 29(4):1603826, 2017.

Appendix A

Calculating Volume-to-Surface Ratio

To generalize the calculation of the ratio of bulk atoms to surface atoms, let us consider a model crystal of length, width, and height $\mathcal{L}$ (Figure A.1). We ascribe to this crystal two regions: the outer shell, described as the surface, and the inner volume, referred to as the bulk. The thickness of the surface may be described as an integer number of lattice constants $n_s a$, where n_s is an integer and a is the lattice constant. If we may confidently say that surface effects are negligible 5 layers beneath the surface, then our model crystal's surface thickness is $T_s = 5a$, where a is the lattice constant of the crystal (on the order of one or several angstroms).

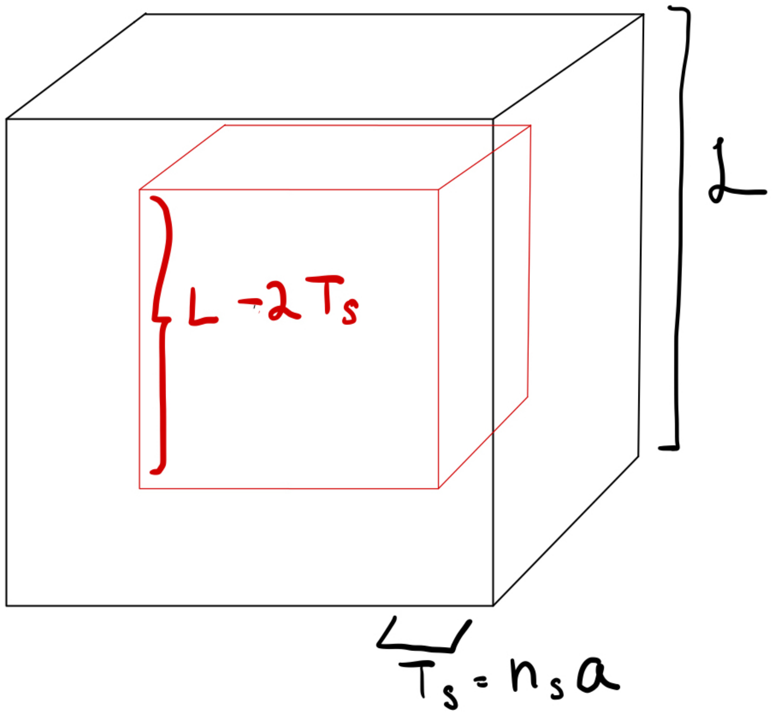

Figure A.1: A crystal of uniform length, width, and height $\mathcal{L}$.

The side length of the inner bulk is then $\mathcal{L} - 2T_s$, as seen in Figure A.1. The volume of our bulk is then simply

$$V_{bulk} = (\mathcal{L} - 2T_s)^3.$$

Meanwhile, the surface's volume would be the entire crystal's volume less the bulk volume:

$$V_{\text{surf}} = V - V_{bulk} = \mathcal{L}^3 - (\mathcal{L} - 2T_s)^3.$$

This would make our bulk-to-surface ratio

$$R = \frac{(\mathcal{L} - 2n_s a)^3}{\mathcal{L}^3 - (\mathcal{L} - 2n_s a)^3}$$

. For a crystal length of 1 µm, a lattice constant of (taking sodium chloride for an example) 2.8 Å, and assume a surface thickness of 5 lattice constants, we get a ratio of

$$R = \frac{(1\mu\text{m} - 1.5\text{nm})^3}{1\mu\text{m}^3 - (1\mu\text{m} - 1.5\text{nm})^3} = 120 : 1.$$

If our crystal's length was 1 mm^3, the surface-to-volume ratio balloons to 120,000:1. Since the atomic lengths are the same throughout the crystal, these volume ratios are equal to the ratio of atoms in the respective regions.

Similar ratios are achieved for spherical crystals of diameters 1 µm and 1 mm, respectively.